Journal of Earthquake and Tsunami, Vol. 4, No. 4 (2010) 285–319

DOI: 10.1142/S1793431110000893

World Scientific
www.worldscientific.com

# THE 1958 LITUYA BAY LANDSLIDE AND TSUNAMI — A TSUNAMI BALL APPROACH

STEVEN N. WARD* and SIMON DAY†

*Institute of Geophysics and Planetary Physics
University of California, Santa Cruz
CA 95064, USA
†Benfield UCL Hazard Research Center
University College London
London, United Kingdom

Accepted 16 May 2010

Many analyses of tsunami generation and inundation solve equations of continuity and momentum on fixed finite difference/finite element meshes. We develop a new approach that uses a momentum equation to accelerate bits or balls of water over variable depth topography. The thickness of the water column at any point equals the volume density of balls there. The new approach has several advantages over traditional methods: (1) by tracking water balls of fixed volume, the continuity equation is satisfied automatically and the advection term in the momentum equation becomes unnecessary. (2) The procedure is meshless in the finite difference/finite element sense. (3) Tsunami balls care little if they find themselves in the ocean or inundating land. We demonstrate and validate the tsunami ball method by simulating the 1958 Lituya Bay landslide and tsunami. We find that a rockslide of dimension and volume ($3 - 6 \times 10^7 \mathrm{m}^3$) generally consistent with observations can indeed tumble from 200–900 m height on the east slope of Gilbert Inlet, splash water up to $\sim 500$ m on the western slope, and make an impressive tsunami running down the length of the fiord. A closer examination of eyewitness accounts and trimline maps, however, finds a "rockslide only" tsunami somewhat lacking in size outside of Gilbert Inlet. This discrepancy, coupled with fact that $\sim 3 \times 10^8$ m$^3$ of sediment infilled the deepest parts of Lituya Bay between 1926 and 1959, suggests that the source of the 1958 tsunami was not one landslide, but two. The initial rockslide generated the famous big splash and cratered the floor in front of Lituya Glacier. We propose that the impact of the rockslide destabilized the foundation of the Glacier and triggered a second larger, but slower moving subglacier slide. The subglacier slide induced the fresh normal faults on the collapsed glacier above, helped to bulk up the rockslide tsunami outside of Gilbert Inlet, and supplied most of the infill evident in post-1958 bathymetric charts.

*Keywords*: Lituya Bay landside; tsunami ball approach.

## 1. Review of the 1958 Event. Above Sea Level Evidence and Past Models

The July 9, 1958 landslide-generated wave in Lituya Bay, Alaska is famous for achieving the highest runup ($\sim 525$ m) of any known tsunami [Miller, 1960]. The inundation produced by this wave, as with previous smaller ones that happened there in historical time, was well mapped by the destruction of the coniferous forest

that grew around the bay. Tsunami-cut "trimlines" from 1958 remain visible 50 years later. Eyewitness accounts provided by survivors on fishing boats caught in the bay paint vivid details of the tsunami in action [Miller, 1960].

The 1958 tsunami was associated with a M7.9 earthquake on the Fairweather Fault that runs along the head of the NE-SW trending T-shaped estuary (Fig. 4). Lituya is a fjord type bay, greatly deepened by glacial erosion. A 1942 chart [U.S. Coast and Geodetic Survey, 1942] records its maximum depth at 220 m. At that time, much of the bay floor sounded to 150–180 m, rising steeply to the shores in U-shaped profiles typical of glaciated fjords. Major temperate glaciers enter the bay at its NW and SE terminations (Gilbert Inlet and Crillon Inlet, respectively). In 1958, Lituya Glacier in Gilbert Inlet was of tidewater type with deep water along its front. Proglacial and subglacial sediment carried by laden meltwater flowing under the ice feed prograding deltas that have progressively infilled the arms of the T. At the bay's seaward end, La Chaussee spit partly closes off the fiord. The sandspit developed on a shallow sill [U.S. Coast and Geodetic Survey 1942, 1969, 1990] and 6 m/s tidal currents over it [U.S. Coast and Geodetic Survey, 1952] transport shallow marine shelf sediment into the deep water of the bay.

Based on photographs of the cliffs around the head of the bay before and after the earthquake, Miller [1960] concluded that seismic shaking triggered a large rockslide from the northeastern wall above the termination of the Lituya Glacier as well as smaller rockslides from the cliffs above the glacier to the north. Miller [1960] appraised the volume of the main rockslide, with its crown some 900 m above sea level, at $3 \times 10^7\,\mathrm{m}^3$; although he states that he was only able to fix roughly the thickness and area of the preslide mass partly because the slide scar continually expanded through the period of his observations. The triggered rockslide apparently fell at high velocity onto the tip of the Lituya Glacier, truncating its nose and removing proglacial delta sediments in front (Figs. 1(a) and 1(b)). The famous 525 m run-up took place on the facing slope of Gilbert Head as water ejected by the rockslide impact ran upslope as a surge or splash. Mapped run-ups elsewhere around the bay ranged up to 220 m, near Mudslide Creek on the south side of the main arm facing Lituya Glacier. Maximum inundation distance reached 1400 m on flat ground at Fish Lake on the north side of the bay, near the entrance.

Miller also documented changes to Lituya Glacier itself, including several arcuate fractures and south-facing faults extending 1.5 km north from the new glacier front. These fractures and faults cut flow bands of debris on the glacier surface (Fig. 1(b)) and so they must have formed in the earthquake or soon after. We interpret the fractures as evidence that several 100 m of the glacier north of the truncated front subsided by tens of meters at the time of the rockslide, possibly due to removal of foundation material.

Survivors on two small fishing boats anchored near the mouth of the bay confirm that the tsunami sourced in Gilbert Inlet. Although the rockslide itself was not

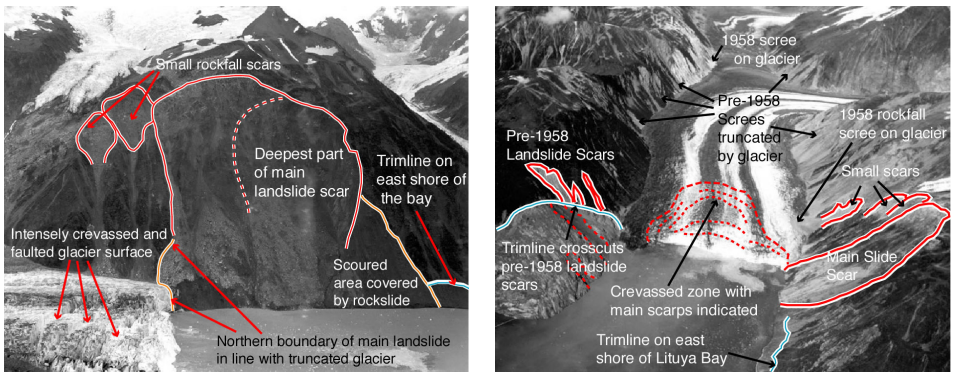


(a) (b)

Fig. 1. Photos of the rockslide scar and Lituya glacier by Millller [1960] with our interpretations. (a) Face-on NE view of rockfall scar and broken tip of Lituya glacier. (b) NW view up the Lituya glacier axis. Red dashed lines trace fresh normal fault scarps on the glacier surface. Diagonal trimline on Gilbert Head as mapped by Miller [1960] is shown in blue.

visible from the boats, the eyewitnesses noted a violent disturbance at the mouth of Gilbert Inlet between 1 and 2-1/2 minutes after the first felt shaking from the earthquake. They described the disturbance as "like an explosion, or glacier sluff" or a "jumping and shaking" mass of fragmented ice, from which the first large wave emerged and propagated down the bay. No drawdown preceded the first wave. The witnesses estimated the wave's height in deep water along the center of the bay at 15–30 m as it engulfed Cenotaph Island, and diminishing somewhat as it reached the boats. Travel time from first sighting of the wave to when it reached the boats was 2-1/2 or 4 min (150 to 250 s, approximately). Many "steep, sharp" (short period) waves up to several meters high arrived after the first large wave but no noticeable trough followed the main crest.

According to Miller [1960], a 1:1000 scale model of Lituya Bay with different slide sources was constructed by Wiegel, but we have not found any documents from this investigation. More recent experiments include two-dimensional [Fritz *et al.*, 2001; Fritz, 2002] and three-dimensional [Fritz *et al.*, 2009] gravel landslides pneumatically accelerated into a wave tank. Numerical attempts at modeling the famous 525 m run-up include Mader [1999] and Mader and Gittings [2002]. None of these works gave much stock to reproducing the eyewitness observations or tsunami inundation patterns, particularly outside of Gilbert Inlet.

To model the 1958 Lituya Bay event, we expand and blend previous research that considered: (1) the subaerial landslide from the May 18th 1980 collapse of Mount St. Helens [Ward and Day, 2006], (2) the inundation stage of open ocean tsunamis [Ward and Day, 2008] and (3) the surge patterns driven by hurricane winds [Ward, 2009]. We intend to examine both the tsunami and the landslide source with the aim of evaluating whether the subaerial rockslide alone could have parented a wave with the known characteristics.

## 2. Tsunami Ball Approach

Traditionally, tsunami generation, local propagation, and inundation have been computed using finite difference or finite element methods on a fixed mesh. This article develops a new approach based on Ward and Day [2008] who computed wave run-up and inundation using "tsunami balls." Simply, tsunami balls are bits of water accelerated over a three-dimensional surface. The volume density of balls at any point equals the thickness of the water column there.

Let $\hat{\mathbf{x}}$ and $\hat{\mathbf{y}}$ directions be east and north in the horizontal plane and $\hat{\mathbf{z}}$ be up. At vector position $\mathbf{r} = (x, y)$, let still water depth to seafloor be $h(\mathbf{r})$ measured positive downward and the perturbation of the surface about the still water level be $\zeta(\mathbf{r}, t)$ measured positive upward (Fig. 2). Common tsunami calculations for earthquake and landslide-generated tsunami [Satake, 1995; Lynett and Liu, 2003; Satake, 2007; Titov and Gonzalez, 2007] solve nonlinear, long wave continuity, and momentum equations for variation in water column thickness $H(\mathbf{r}, t) = h(\mathbf{r}) + \zeta(\mathbf{r}, t)$ and depth averaged horizontal water velocity $\mathbf{v}(\mathbf{r}, t)$ at fixed mesh nodes

$$\frac{\partial H(\mathbf{r}, t)}{\partial t} = -\nabla_h \bullet [\mathbf{v}(\mathbf{r}, t) H(\mathbf{r}, t)] \tag{1}$$

and

$$\frac{\partial \mathbf{v}(\mathbf{r}, t)}{\partial t} = -\mathbf{v}(\mathbf{r}, t) \bullet \nabla_h \mathbf{v}(\mathbf{r}, t) - g \nabla_h \zeta(\mathbf{r}, t) \tag{2}$$

where $g$ is the acceleration of gravity and $\nabla_h$ is the horizontal gradient.

Replacing this approach, we intend to employ a momentum equation to accelerate $N$ tsunami balls around on a surface of varying topography. The tsunami balls (perhaps better thought of as constant volume water columns) are treated as point masses and the wave height $\zeta(\mathbf{r},\ t)$ at any location is calculated from the volume density of near-by tsunami balls:

$$\zeta(\mathbf{r}, t) = \sum_{j=1}^{N} V_j \ A(\mathbf{r}, \mathbf{r}_j(t)) - h(\mathbf{r}) \tag{3}$$

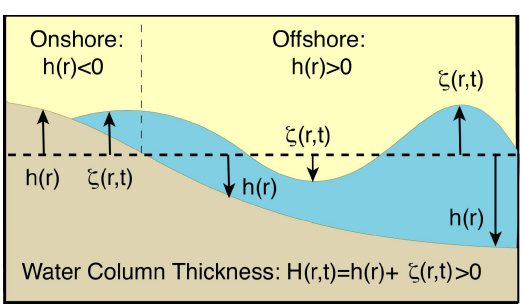


Fig. 2. Geometry for tsunami ball calculations. Still water depth $h(r)$ is measured positive downward. The perturbation of the water surface about still water $\zeta(r, t)$ is measured positive upward.

In (3), $V_j$ is the fixed water volume of the $j$th ball, $\mathbf{r}_j(t)$ is the ball's location at time $t$, and $A(\mathbf{r}, \mathbf{r}_j(t))$ is an averaging function with $\mathrm{m}^{-2}$ units such that when integrated over all $(x, y)$ space

$$\int A(\mathbf{r}, \mathbf{r}')\mathbf{dr}' = 1 \tag{4}$$

The advantages of a tsunami ball approach to wave generation and inundation are three:

(1) Because we track water balls of fixed volume, the continuity equation (1) is satisfied automatically. In locations where the volume density (3) of balls grows, the water column thickness increases. In locations where the volume density drops, the thickness of the water column falls.

(2) The tsunami ball procedure is meshless. Meshless applications offer a huge simplification over finite difference/finite element methods in that one can download a coastal DEM and start the calculation immediately without having to worry about mesh density, node locations, etc.

(3) Tsunami balls care little if they find themselves in the ocean $h(\mathbf{r}) > 0$ or if they have run onto land $h(\mathbf{r}) < 0$ (Fig. 2). Such indifference is made-to-order for inundation applications because it obviates the need for special "dry cell" and "wet cell" behaviors.

Tsunami balls have similarities to wave calculations using smoothed particle hydrodynamics [e.g., Rodgers and Dalrymple, 2008]: both approaches are meshless; both approaches are Lagrangian in that they follow particles; and both approaches derive physical quantities by summing over particle properties weighted by distance smoothing functions. By considering water columns rather than spherical particles, the tsunami ball approach can handle real world-scale problems better than SPH, but at the expense of resolving variations with depth.

### 2.1. *Advection*

As mentioned, many tsunami wave calculations solve (1) and (2) at fixed mesh nodes $\mathbf{r}$. A portion of the change in water velocity at $\mathbf{r}$ as described by (2) represents real accelerations of the water in the vicinity. Another part of the velocity change accounts for the fact that the water particles at $\mathbf{r}$ at time $t$ are not the same ones that will be there at $t + \Delta t$. If the new particles have different velocities than the old ones, $\mathbf{r}$ experiences an apparent (or advected) acceleration. Here, because we intend to track specific bits of water, the advection term $\mathbf{v}(\mathbf{r}, t) \bullet \nabla_h \mathbf{v}(\mathbf{r}, t)$ in (2) falls away. In the tsunami ball approach, quantities like (3), evaluated at fixed locations automatically account for the fact that different tsunami balls contribute to the count at different times so we avoid a numerical differentiation of velocity $\nabla_h \mathbf{v}(\mathbf{r}, t)$.

### 2.2. *Ties to linear tsunami theory*

Equations (1) and (2) describe nonlinear shallow water waves. It is important for us that the driving equations for tsunami balls reproduce linear wave theory when the waves are small, but not be restricted to long waves alone.

Consider an arbitrary three-dimensional tsunami field under classical linear theory in a uniform ocean of depth $h$ at time $t$,

$$\mathbf{u}(\mathbf{r}, z, t) = \mathrm{Re} \int_{\mathbf{k}} \begin{bmatrix} \hat{\mathbf{z}} u_z(\mathbf{k}, \mathbf{r}, z, t) \\ -i\hat{\mathbf{k}} u_h(\mathbf{k}, \mathbf{r}, z, t) \end{bmatrix} d\mathbf{k} \tag{5}$$

where

$$u_z(\mathbf{k}, \mathbf{r}, z, t) = \frac{F(\mathbf{k}) \mathrm{e}^{i(\mathbf{k}\bullet\mathbf{r} - \omega(k)t)}}{4\pi^2} \times \frac{\sin h(k(h-z))}{\sin h(kh)} \tag{6a}$$

$$u_h(\mathbf{k}, \mathbf{r}, z, t) = \frac{F(\mathbf{k}) \mathrm{e}^{i(\mathbf{k}\bullet\mathbf{r} - \omega(k)t)}}{4\pi^2} \times \frac{\cos h(k(h-z))}{\sin h(kh)} \tag{6b}$$

In Eqs. (5) and (6a), $z$ is depth (measured positive down in this section) $\mathbf{k} = k_x\hat{\mathbf{x}} + k_y\hat{\mathbf{y}}$ is waveumber, $k = |\mathbf{k}|$, $\hat{\mathbf{k}} = \mathbf{k}/k$, $\mathbf{dk} = dk_x dk_y$, $F(\mathbf{k})$ is a source spectrum and frequency $\omega(k)$ is

$$\omega(k) = \sqrt{gk \tan h(kh)} \tag{7}$$

We are mostly interested in time and space derivatives of vertical surface displacement

$$u_z(\mathbf{r}, 0, t) = -\xi(\mathbf{r}, t) = \mathrm{Re} \int_{\mathbf{k}} u_z^{\mathrm{surf}}(\mathbf{k}, \mathbf{r}, t) d\mathbf{k} \tag{8}$$

and time and space derivatives of horizontal displacement averaged over depth

$$\bar{\mathbf{u}}_h(\mathbf{r}, t) = \mathrm{Re} \int_{\mathbf{k}} -i\hat{\mathbf{k}} \bar{\mathrm{u}}_h(\mathbf{k}, \mathbf{r}, t) d\mathbf{k} \tag{9}$$

with

$$\bar{\mathrm{u}}_h(\mathbf{k}, \mathbf{r}, t) = h^{-1} \int_0^h u_h(\mathbf{k}, \mathbf{r}, z, t) dz = u_z^{\mathrm{surf}}(\mathbf{k}, \mathbf{r}, t)/kh \tag{10}$$

Under linear tsunami theory, (10) tells us that depth averaged horizontal motion relates simply to vertical motion at the surface. The depth averaged horizontal water velocity in (1–2) is

$$\mathbf{v}(\mathbf{r}, t) = \frac{\partial \bar{\mathbf{u}}_h(\mathbf{r}, t)}{\partial t} = \dot{\bar{\mathbf{u}}}_h(\mathbf{r}, t) = \mathrm{Re} \int_{\boldsymbol{k}} -i\hat{\mathbf{k}} \dot{\bar{\mathbf{u}}}_h(\mathbf{k}, \mathbf{r}, t) d\mathbf{k} \tag{11}$$

In a uniform depth ocean, the linearized version of (1a) becomes

$$\frac{\partial u_z(\mathbf{r}, 0, t)}{\partial t} = h\nabla_h \bullet [\dot{\bar{\mathbf{u}}}_h(\mathbf{r}, t)] \tag{12}$$

Does the linear tsunami field satisfy (12)? If so, then plugging in (5–6) must yield the equality

$$\begin{aligned} -i\omega u_z^{\text{surf}}(\mathbf{k},\mathbf{r},t) &=^{?} h(i\mathbf{k}) \bullet [-i\hat{\mathbf{k}}(-i\omega)\bar{\mathrm{u}}_h(\mathbf{k},\mathbf{r},t)] \\ -i\omega u_z^{\text{surf}}(\mathbf{k},\mathbf{r},t) &=^{?} -i\omega kh\bar{\mathrm{u}}_h(\mathbf{k},\mathbf{r},t) \\ u_z^{\text{surf}}(\mathbf{k},\mathbf{r},t) &=^{?} u_z^{\text{surf}}(\mathbf{k},\mathbf{r},t) \quad \therefore \end{aligned} \tag{13}$$

In (13) we have made use of (10) and the facts that the differential operators transform as

$$\partial/\partial t \Leftrightarrow -i\omega; \quad \nabla_h \Leftrightarrow i\mathbf{k} \tag{14}$$

So, yes, tsunami field (5–6) satisfies the linearized version of the depth averaged equation (1a) even if the tsunami is not a long wave. What about linearized Eq. (2)?

$$\frac{\partial \dot{\bar{\mathbf{u}}}_h(\mathbf{r},t)}{\partial t} = g\nabla_h u_z(\mathbf{r},0,t) \tag{15}$$

Does the linear tsunami field satisfy this? If so, then

$$\begin{aligned} -i\omega[(-i\omega)(-i\hat{\mathbf{k}})\bar{\mathrm{u}}_h(\mathbf{k},\mathbf{r},t)] &=^{?} g(i\mathbf{k})\, u_z^{\text{surf}}(\mathbf{k},\mathbf{r},t) \\ i\omega^2\hat{\mathbf{k}}u_z^{\text{surf}}(\mathbf{r},\mathbf{k},t)/kh &=^{?} (i\mathbf{k})g\, u_z^{\text{surf}}(\mathbf{k},\mathbf{r},t) \\ u_z^{\text{surf}}(\mathbf{r},\mathbf{k},t) &=^{?} k^2 gh\, u_z^{\text{surf}}(\mathbf{k},\mathbf{r},t)/\omega^2 \\ u_z^{\text{surf}}(\mathbf{r},\mathbf{k},t) &=^{?} u_z^{\text{surf}}(\mathbf{k},\mathbf{r},t)\left[\frac{\tan h(kh)}{kh}\right]^{-1} \end{aligned} \tag{16}$$

where use was made of (7) in the final step. No, tsunami field (5)–(6) does not satisfy depth averaged equation (2) unless $kh \ll 1$. Evidently, for our tsunami ball application to reduce to linear theory when the waves are small but not always long, Eq. (2) must be replaced by

$$\frac{\partial \mathbf{v}(\mathbf{r},t)}{\partial t} = -g\nabla_h \zeta_{\text{smooth}}(\mathbf{r},t) \tag{17}$$

where

$$\zeta_{\text{smooth}}(\mathbf{r},t) = \zeta(\mathbf{r},t) * \mathrm{S}(\mathbf{r}) = \int \zeta(\mathbf{r}',t)\mathrm{S}(\mathbf{r}-\mathbf{r}')d\mathbf{r}' \tag{18}$$

and

$$\mathrm{S}(\mathbf{r}) = \mathrm{Re}\int_{\boldsymbol{k}} \frac{\mathrm{e}^{i\mathbf{k}\bullet\mathbf{r}}}{4\pi^2}\frac{\tan h(kh)}{kh}d\mathbf{k} \tag{19}$$

In words, the mean horizontal acceleration of the water column depends on the slope of the surface smoothed over a dimension comparable to the water depth. Short wave ($kh \gg 1$) contributions to the surface slope must accelerate tsunami balls less than longer wave ($kh \ll 1$) contributions if the results are to reproduce linear tsunami theory.

What does $S(\mathbf{r}-\mathbf{r}')$ look like? Equation (19) cannot be evaluated easily, but to the extent that

$$\frac{\tan h(kh)}{kh} \approx \frac{1}{[1+(kh)^2]^{1/2}}; \quad \text{then}$$

$$S(\mathbf{r}-\mathbf{r}') \approx \frac{e^{-|\mathbf{r}-\mathbf{r}'|/h}}{2\pi h|\mathbf{r}-\mathbf{r}'|} \tag{20}$$

Alternatively, to the extent that

$$\frac{\tan h(kh)}{kh} \approx \frac{1}{[1+(kh/\alpha)^2]^{3/2}}; \quad \text{then}$$

$$S(\mathbf{r}-\mathbf{r}') \approx \frac{e^{-\alpha|\mathbf{r}-\mathbf{r}'|/h}}{2\pi(h/\alpha)^2} \tag{21}$$

Equation (20) (Fig. 3, left) better approximates (19) than (21) (Fig. 3, right), but it is unwieldy due the singularity as $|\mathbf{r}-\mathbf{r}'| \to 0$. Equation (21) with parameter $\alpha = 2.5$ works adequately for waves $kh < 2.5$. Slowly adjusting $\alpha$ downward with time, increases smoothing and aids stability (see Sec. 5.3). In either (20) or (21), it is easy to see that if $h = h(\mathbf{r})$, deep water locations will be smoothed over a larger area than shallow water locations. Either $S(\mathbf{r}-\mathbf{r}')$ with $h = h(\mathbf{r})$, has units $m^{-2}$, integrates to unity, and reduces to a delta function as $h(\mathbf{r})$ gets small. $S(\mathbf{r}-\mathbf{r}')$ (21) will serve as the smoothing function $A(\mathbf{r},\mathbf{r}')$ in (3).

### 2.3. *Tsunami ball flow chart*

The tsunami ball method distills to six flow chart steps.

**(A)** Distribute $N$ tsunami balls over the water area at initial positions $\mathbf{r}_j$ with regular spacing $\Delta x \Delta y$.

**(B)** Assign each ball a zero initial velocity and a constant volume $V_j = \Delta x \Delta y h(\mathbf{r}_j)$ based on still water depth at the site $h(\mathbf{r}_j)$.

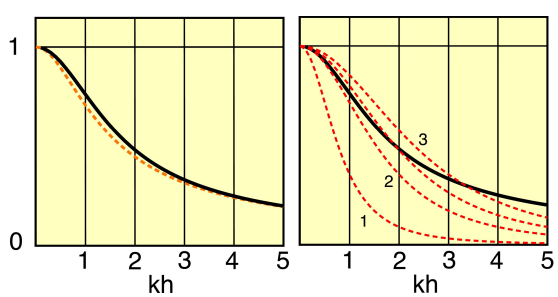


Fig. 3. Plot of $\tan h(kh)/kh$ (solid lines) and approximations (20) (left) and (21) (right) with $\alpha = 1, 2, 2.5$, and 3.

**(C)** Evaluate the smoothed water surface at time $t$ on a fixed set of grid points $\mathbf{r}_g$

$$\zeta_{\text{smooth}}(\mathbf{r}_g, t) = \sum_{j=1}^{N} V_j S(\mathbf{r}_g - \mathbf{r}_j(t)) - h(\mathbf{r}_g) \tag{22}$$

**(D)** Accelerate each tsunami ball for a short duration $\Delta t$ using

$$\frac{\partial \mathbf{v}_j(t)}{\partial t} = -g\nabla_h \zeta_{\text{smooth}}(\mathbf{r}_g, t) - C_d|\mathbf{v}_j(t)|\mathbf{v}_j(t) \tag{23}$$

The $\mathbf{r}_g$ here is the grid point closest to the ball's position.

(**E**) Update the ball position,

$$\mathbf{r}_j(t + \Delta t) = \mathbf{r}_j(t) + \mathbf{v}_j(t)\Delta t + \frac{\Delta t^2}{2}\frac{\partial \mathbf{v}_j(t)}{\partial t} \tag{24}$$

ball velocity,

$$\mathbf{v}_j(t + \Delta t) = \mathbf{v}_j(t) + \Delta t \frac{\partial \mathbf{v}_j(t)}{\partial t} \tag{25}$$

and time $t = t + \Delta t$.

**(F)** Here you might return to Step (D) several times keeping the surface fixed at its most recent evaluation (inner loop); or, return to Step (C) to compute a fresh surface (outer loop).

Regardless if the tsunami ball is in water or has been tossed onto land, steps (C) to (F) hold. Note that acceleration (23) includes a dynamic drag to control balls that might encounter unreasonably steep surface gradients and "run away". For tsunami balls in the ocean, $C_{\text{d}} = 0.0002/\text{m}$. When tsunami balls blow onto land, they encounter more resistance to flow so $C_{\text{d}} = 0.0006/\text{m}$ there. To stabilize the calculation, we include additional damping measures given below.

What in the flow chart makes the tsunami? Waves get stirred if the depth of still water $h(\mathbf{r})$ in (22) becomes a function of time

$$h(\mathbf{r}) \Rightarrow h_0(\mathbf{r}) + \Delta h(\mathbf{r}, t) \tag{26}$$

where $h_o(\mathbf{r})$ is the original value in flow chart step (B) and $\Delta h(\mathbf{r}, t)$ is the bottom uplift or subsidence due to a earthquake or passing landslide. We calculate $\Delta h(\mathbf{r}, t)$ from the landslide simulations in the next section.

## 3. Granular Landslide Simulation

In contrast to existing landslide models for tsunami generation [Slingerland and Voight, 1979; Jiang and LeBlond, 1993; Lynett and Liu, 2003; Satake, 2007], we build landslides following steps surprisingly similar to those in the tsunami flow chart above. In fact, tsunami run-up and inundation is just a special landslide case — a "water landslide" if you will [Ward and Day, 2006, 2008]. For Steps (A) and (B) in a landslide flow chart, the slide bits all have equal volume $V^{\text{slide}}$and distribute

over the landslide area with a density such as to reproduce the prescribed spatial thickness of the slide mass. The top surface of the landslide and its thickness is computed in Step (C) again by (22), but now with a position independent smoothing function

$$\mathrm{S}(\mathbf{r}-\mathbf{r}') = \frac{\mathrm{e}^{-[|\mathbf{r}-\mathbf{r}'|/L]^2}}{\pi L^2} \tag{27}$$

with $L = 50\,\mathrm{m}$. In Step (D), the landslide bits accelerate by

$$\begin{aligned}\frac{\partial \mathbf{v}_j(t)}{\partial t} &= -g\nabla_h \left[ V^{\mathrm{slide}} \sum_{j=1}^{N} S(\mathbf{r}_g - \mathbf{r}_j(t)) - h(\mathbf{r}_g) \right] - C_\mathrm{d}|\mathbf{v}_j(t)|\mathbf{v}_j(t) - gC_\mathrm{b}\hat{\mathbf{v}}_j(t) \\ &= g\nabla_h h(\mathbf{r}_g) - g\nabla_h \zeta_{\mathrm{slide}}(\mathbf{r}_g, t) - C_\mathrm{d}|\mathbf{v}_j(t)|\mathbf{v}_j(t) - gC_\mathrm{b}\hat{\mathbf{v}}_j(t) \end{aligned} \tag{28}$$

The first term on the right-hand side represents the acceleration of the slide over fixed topography (the basal surface). The second term is the acceleration due to the evolving shape of the slide mass itself. We call this the "self-topography force." Self-topography forces pull apart and flatten landslide masses. We replicate the transition between block-like and flow-like behaviors seen in landslides by easing in self-topography over a duration roughly equal to the time it takes for the mass to move one slide length. Increasing self-topography forces with time corresponds to a decreasing cohesion of the landslide mass as it fragments. The only other term in (28) not present in (23) is $C_\mathrm{b}$, a unitless basal friction.

## 4. Stabilization

We wish to stabilize the calculation, but not damp events so strongly as to induce "vanishing tsunami syndrome" — an ailment that we diagnose in many purely numerical approaches. For a guide, we compute and track the total kinetic energy of the balls. Total kinetic energy of the water waves should slowly trend downward with time. Run-away kinetic energy sounds the alert to increase damping.

### *Increase smoothing with time*

By decreasing $\alpha$ in (21), the water wave field becomes smoother as short wavelength (high $kh$) elements face stronger filtering (Fig. 3, *right*). Decreasing $\alpha$ over time nicely sires steep wave fronts at the initial rockfall, but reduces unstably growing waves and kinetic energy long afterward.

### *Employ one way gravity*

"One-way" gravity also selectively damps unwanted waves. One-way gravity picks the value of $g$ in momentum equation (23) at each location and time based on the current velocity $\mathbf{v}_\mathrm{j}(t)$ of the tsunami ball being accelerated and the gradient of the

surface slope $-\nabla_h\zeta(\mathbf{r}_g,t)$ at the nearest grid location. In our application we want to damp small random ripples but not hinder larger waves, so

$$-\nabla_h\zeta(\mathbf{r}_g,t)\bullet\mathbf{v}_j(t)<0;\quad \text{then } g=9.8\,\text{m/s} \tag{29a}$$

$$-\nabla_h\zeta(\mathbf{r}_g,t)\bullet\mathbf{v}_j(t)>0\quad\text{and}\quad|\zeta(\mathbf{r}_g,t)|>1\text{m};\quad\text{then } g=9.8\,\text{m/s} \tag{29b}$$

$$-\nabla_h\zeta(\mathbf{r}_g,t)\bullet\mathbf{v}_j(t)>0\quad\text{and}\quad|\zeta(\mathbf{r}_g,t)|<1\text{m};\quad\text{then } g=0.05^*\ 9.8\,\text{m/s} \tag{29c}$$

In words, if acceleration $-g\nabla_h\zeta(\mathbf{r}_g,t)$ opposes ball velocity $\mathbf{v}_j(t)$ (29a) or if the surface deflection $|\zeta(\mathbf{r}_g,t)|$ is large, as in a passing wave, gravity acts in full force (29b). If acceleration $-g\nabla_h\zeta(\mathbf{r}_g,t)$ reinforces velocity $\mathbf{v}_j(t)$ and the surface deflection is small, as in unwanted ripples, reduced gravity acts (29c). Think of a playground swing — by fully opposing the upswing (29a) and by hardly accelerating part of the downswing (29c), one-way gravity effectively damps the oscillation.

## 5. 1958 Lituya Bay Landslide Tsunami — Rockslide Source

Our landslide tsunami simulations involve two stages. The first stage computes a slide history $\Delta h(\mathbf{r},t)$. The second stage feeds this history into the tsunami ball calculation to induce waves. In this partially coupled procedure, the landslide affects

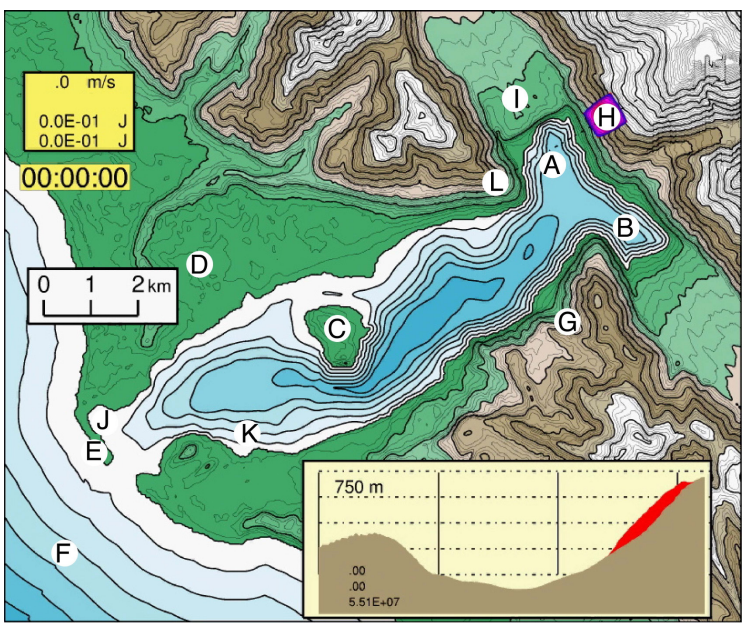


Fig. 4. Lituya Bay location map. Bathymetric contours are 30 m and represent our estimate of the pre-1958 bathymetry. On land, light and dark contours are 25 and 100 m, respectively. Location codes: (A) Gilbert Inlet, (B) Crillon Inlet, (C) Cenotaph Island, (D) Fish Lake, (E) La Chaussee Spit, (F) Pacific Ocean, (G) Mudslide Creek, (H) Rockslide, (I) Lituya Glacier, (J) *Badger* anchorage, (K) *Edrie* anchorage, and (L) Gilbert Head. Cross-section at bottom right projects along dotted line from Gilbert Head, through Gilbert Inlet and the Rockslide.

the tsunami, but not vice versa. Both the landslide and tsunami simulations ran on a modern-day topographic grid at 1 arc second (30 m) spacing [USGS EarthExplorer http://earthexplorer.usgs.gov]. Our Lituya Bay bathymetry approximates Miller's [1960] map derived from a 1942 chart and 1926 survey [U.S. Coast and Geodetic Survey, 1942] — the last pre-1958 survey of the bay (Fig. 8, top). Primary outputs of the simulation include the history and shape of the landslide and wave, their kinetic and potential energies, and on-land inundation coverage. We validate the whole procedure by comparing simulation output with observed features of the 1958 event and its effects, ranging from changes in the bathymetry of the bay attributed to landslide deposits, through eyewitness observations of the tsunami, to the exceptionally complete inundation information provided by Miller's mapping.

### 5.1. *Landslide parameters and landslide evolution*

The area of the Lituya Bay rockslide is moderately well fixed by Miller [1960, 1964] (Fig. 1(a)); however, the volume and thickness distribution of the material are less certain. Miller [1960] proposed a volume of $3 \times 10^7$ m$^3$. We selected a somewhat larger value of $5.5 \times 10^7$ m$^3$ (motivation given below). Mounding the material in prismatic fashion over our slide area ($0.456 \times 10^6$ m$^2$) gave the rockslide mean and peak thickness of 120 m and 200 m. The landslide bits took a basal drag coefficient $C_\mathrm{b}$ from a random distribution with mean 0.005 and standard deviation 0.00125. Dynamic drag $C_\mathrm{d}$ coefficient was $5 \times 10^{-4}$/m for slide bits on land and $20 \times 10^{-4}$/m for slide bits in water. Self-topographic forces eased in over 60 s. The rockslide consisted of 10,000 bits stepped at 1 s intervals.

Gravitational potential energy lost by a landslide is

$$\begin{aligned} E_g^{\mathrm{slide}}(t) &= \rho_s g \int \left[\frac{T(\mathbf{r},t) + T_0(\mathbf{r})}{2}\right] [T(\mathbf{r},t) - T_0(\mathbf{r})] d\mathbf{r} \\ &= \rho_s g \int (1/2)[T^2(\mathbf{r},t) - T_0^2(\mathbf{r})] d\mathbf{r} \\ &= \rho_s g \int [T_0(\mathbf{r})[T(\mathbf{r},t) - T_0(\mathbf{r})] + (1/2)[T(\mathbf{r},t) - T_0(\mathbf{r})]^2] d\mathbf{r} \end{aligned} \quad (30\text{a–c})$$

where $\rho_\mathrm{s}$ is slide density (2.5 g/cm$^3$), $\mathrm{T}(\mathbf{r},t)$ and $\mathrm{T}_0(\mathbf{r})$ are the current and initial topographic elevations, respectively. The elevations include the slide mass but not the water. The second integral in (30c) is positive, but the sum has to be negative if the slide releases energy. For fixed slide volume $\int [T(\mathbf{r},t) - T_0(\mathbf{r})] d\mathbf{r} = 0$, so the reference level for topography (e.g., sea level) is irrelevant. The kinetic energy of the slide equals the sum of the kinetic energy of its individual bits

$$E_k^{\mathrm{slide}}(t) = (1/2)\rho_s V^{\mathrm{slide}} \sum_{j=1}^{N} v_j^2(t) \quad (31)$$

$-E_g^{\text{slide}}(t)$ (30) quantifies the total energy available for all aspects of the process. In an energetically acceptable simulation, $-E_g^{\text{slide}}(t)$ must always exceed $E_k^{\text{slide}}(t)$ plus the kinetic $E_k^{\text{water}}(t)$

$$E_k^{\text{water}}(t) = (1/2)\rho_w \sum_{n=1}^{N} V_n^{\text{water}} v_n^2(t) \tag{32}$$

and potential energy change $E_g^{\text{water}}(t)$.

$$E_g^{\text{water}}(t) = \rho_w g \sum_{n=1}^{N} V_n^{\text{water}} [\mathrm{T}(\mathbf{r}_{\mathrm{g}}(t)) - \mathrm{T}_0(\mathbf{r}_g(0))] \tag{33}$$

of the water. In (33), the $\mathbf{r}_{\mathrm{g}}(t)$ and $\mathbf{r}_{\mathrm{g}}(0)$ are the grid points closest to $n$th ball's position at time $t$ and $t = 0$. Part of potential energy (33) associates with dynamic wave action and part accounts for the fact that the water in the fiord ends up at a higher elevation than it started having been displaced by landslide. We take care to list quantities (30–33) in our simulations.

Figures 5(a) and 5(b) snap seven shots of the rockslide simulation. (All of the simulations presented in this article are accompanied by Quicktime movie animations. See Appendix A. View the Quicktime movie version of Fig. 5 at http://es.ucsc.edu/∼ward/lituya-slide.mov). The information in the yellow box in Fig. 5 includes the mean speed of the moving slide, the number of moving slide bits, the total number of slide bits, and $E_k^{\text{slide}}(t)$ (31) and $E_g^{\text{slide}}(t)$ (30).

⇒ $T$: 0–20 s (Fig. 5(a), Frames A, B): From its original elevation between 200 m and 900 m, the slide accelerates to 66 m/s as it slams down into Gilbert Inlet. The slide has not deformed much yet because self-topography has just begun to take effect.

⇒ $T$: 20–40 s (Fig. 5(a), Frame C): The slide traverses the 1 km width of Gilbert Inlet and slows to 21 m/s. The mass deforms rapidly from this point forward.

⇒ $T$: 40–60 s (Fig. 5(b), Frames A, B): By now, the slide mass has deflected from the western slope of Gilbert Inlet and has begun to flow southward toward the main fiord at 20 m/s. Note that no part of the slide reached more than 100 m up onto the western shore of the Inlet.

⇒ $T$: 60–600 s+ (Fig. 5(b), Frames C, D): The rockslide, now fully evolved into a debris flow about 40 m thick, courses toward main arm of the fiord at 10–15 m/s. In 15 min more, the debris will traverse the length of the fiord and deposit at its deepest point south of Cenotaph Island. The small rockslide volume reduces the depth of the bay there by just a few meters.

Total rockslide potential energy is $9.7 \times 10^{14}$ J. Its peak kinetic energy is $4.1 \times 10^{14}$ J and the ratio of kinetic energy to potential energy lost tops 85%, seven seconds into sliding.

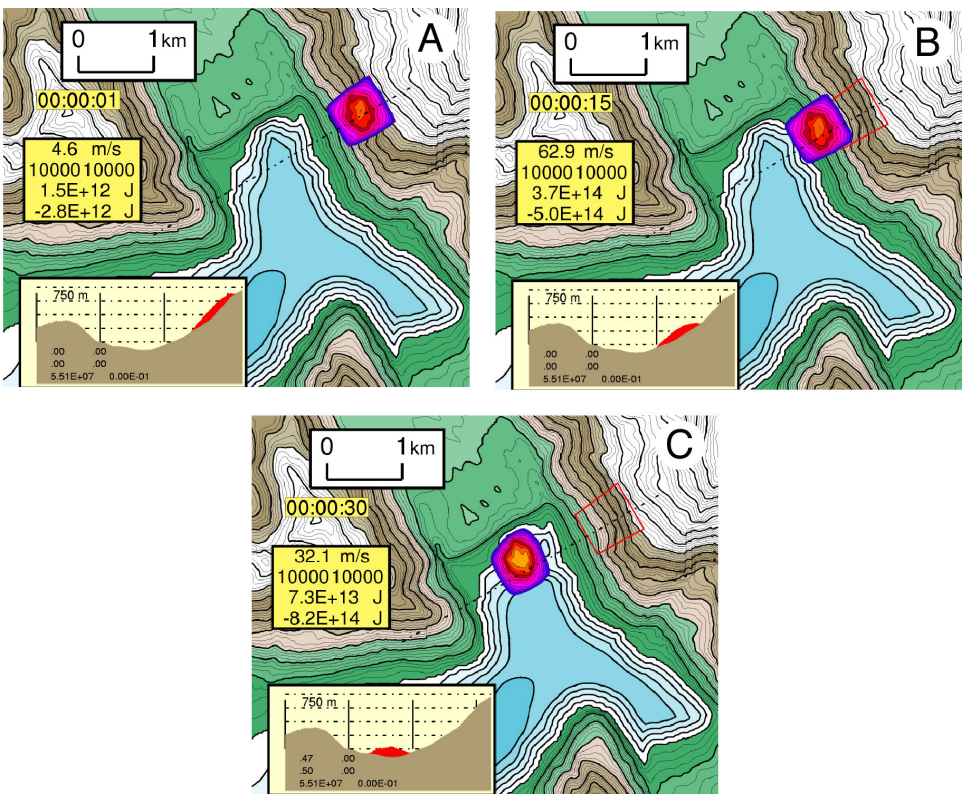


Fig. 5(a). Rockslide simulation 0–30 s. Cross-section in lower left graphs slide thickness and location cut along the dashed line. Contour interval of slide thickness is 20 m starting at 20 m. Maximum initial thickness is 200 m.

### 5.2. *Wave simulation for the rockslide source*

To run the tsunami simulation, 4.4 million tsunami balls were distributed at 3 m intervals over all wet locations in Lituya Bay and out to just beyond its mouth. We updated tsunami ball position (24) and velocity (25) every $\Delta t = 0.05$ s in the inner loop and refreshed the water surface every 1 s in the outer loop. Passing the outer loop also updated the tsunami-driving changes in the ocean floor elevation $\Delta h(\mathbf{r}, t)$ from the rockslide simulation. We printed a movie frame at 2 s intervals.

Figures 6(a) and 6(b) show the Rockslide tsunami in two-dimensional map view. (Quicktime movie at http://es.ucsc.edu/∼ward/lituya2d.mov).

⇒ $T$: 0–30 s (Fig. 6(a): Frame A): The initial high-speed impact of the rockslide scoops up water into a 150-m-high pile and drives it westward.

⇒ $T$: 30–60 s (Fig. 6(a): Frame B): The initial impulsive wave breaks upon impacting the western shore of Gilbert Inlet. The collapse of the giant pulse provides a tremendous kick of kinetic energy to the forward elements of the wave. The kinetic energy boost tosses a thin sheet of water up to ∼500 m elevation on the east face

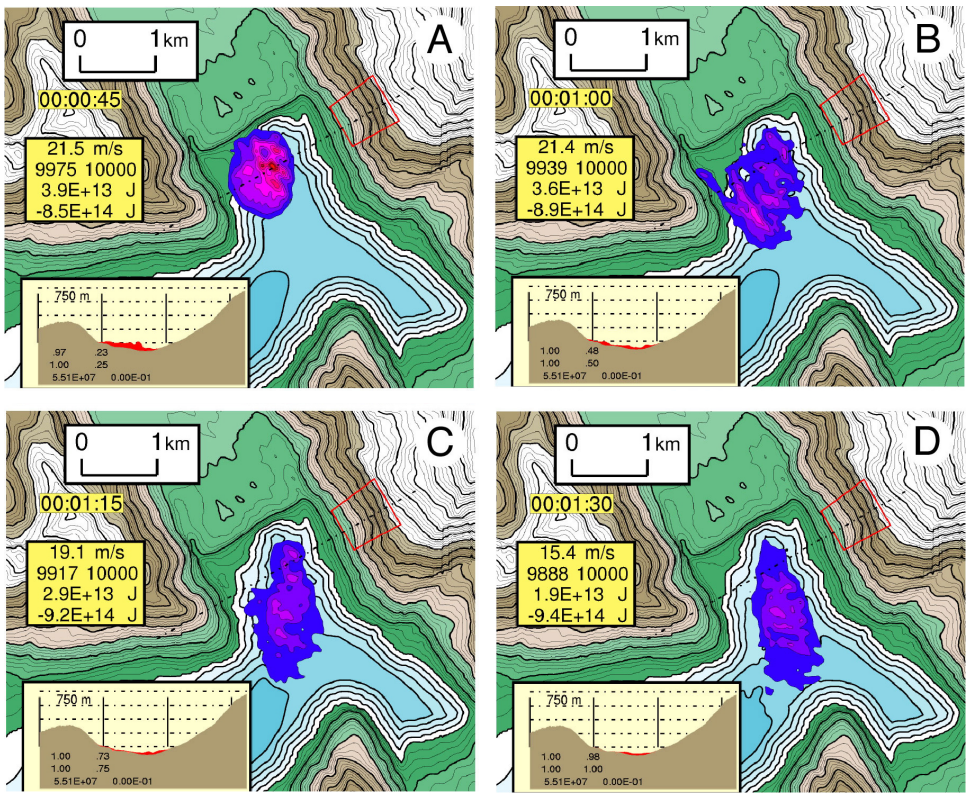


Fig. 5(b). Rockslide simulation $T = 45, 60, 75$, and 90 s. After deflecting off of the western slope of Gilbert Inlet, the rockslide — now a debris flow — thins and slowly runs down toward the main fiord.

of Gilbert Head. The legendary "525 m high" Lituya Bay Tsunami is best characterized as a big splash — the wave itself never exceeded 200 m thickness in water or 100 m thickness on land (see inset Fig. 5).

$\Rightarrow T$: 1–2 min (Fig. 6(b): Frames C, D): Water retreats back down from the high elevations and the wave refracts westward down the main axis of the bay, inundating only moderately the south side of Gilbert Head. 35 m high waves generated by the southern flank of the rockslide bear down on the Bay's south shore.

$\Rightarrow T$: 2–3 min (Fig. 6(a): Frame D and Fig. 5(b): Frame A): Water runs up over 150 m at locations east and west of Mudslide Creek (Location G, Fig. 4). The wave then reflects off of the south shore and courses northwest following behind the directly refracted wave.

$\Rightarrow T$: 3–5 min (Fig. 6(b): Frames B, C): A 20 m high wave strikes the east face of Cenotaph Island, running up on land to 40 m. The tsunami splits here — part travels via the shallow water north of the Island and part travels via deeper water to the south.

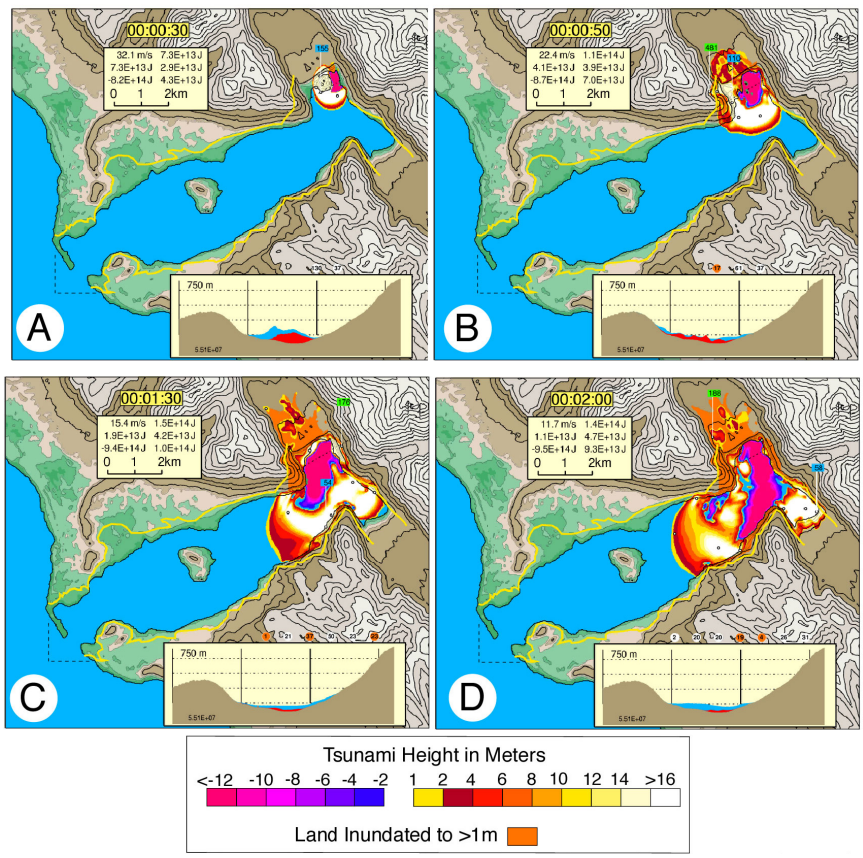


Fig. 6(a). Rockfall Tsunami simulation at $T = 30\,\text{s}$, 50 s, 1–1/2 min-and 2 min. In Frame B, the wave run, up reaches 481 m height. The yellow line is Miller's mapped trimline. Note how it cuts diagonally across contours on the east and west sides of Gilbert Head (Frame A).

$\Rightarrow$ $T$: 5–6 min (Fig. 6(b): Frame D): The 15 m high southern branch of the wave whips around Cenotaph Island in a boomerang-like style, bends northward, and joins forces with the slower-going wave at the northwest corner of the Island. The combined waves peak to 22 m and run in deeply on North Shore near Fish Lake (Location D, Fig. 4). Expulsion of the main wave draws down water to $-10$ m along the south and southeast sides of the bay, briefly exposing areas of the seabed.

$\Rightarrow$ $T$: 6–7+ min (Fig. 6(b): Frames E, F): Waves of 10 m height approach La Chaussee Spit. Waves of 5 m size pass over and escape to sea.

Peak potential and kinetic energies for the water were $1.1\times10^{14}$ J and $5.2\times10^{13}$ J, respectively. Peak total energy of the water amounted to $1.8\times10^{14}$ J — 19% of the $0.97\times10^{15}$ J rockslide energy.

Figure 7 pictures the rockslide tsunami in a three-dimensional style. (Quicktime movie at http://es.ucsc.edu/∼ward/lituya3d.mov). To help visualize the sequence

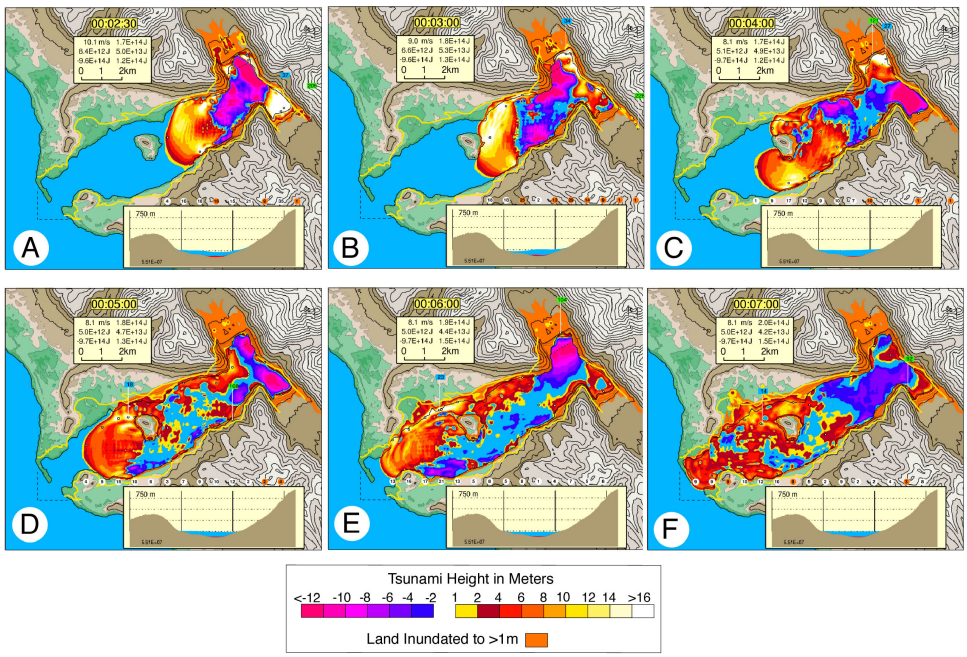


Fig. 6(b). Tsunami for Rockfall source at $T = 21/2, 3, 4, 5, 6$, and 7 min.

of events, we portray the topography and tsunami with considerable vertical exaggeration (Frame A). Note the large westward traveling initial pulse and the smaller-sized southbound waves (Frame B). Breaking and collapse of the initial pulse drives a thin sheet of water $\sim$500 m up on west shore of Gilbert Inlet (Frame C). Main wave refracts westward around Gilbert Head and also attacks the south shore (Frame D). The south shore wave reflects and travels northwest obliquely behind the more direct wave (Frames E–F). The reflected wave contacts the north shore east of the Island while main wave encounters the Island. Please view the movie link above where you can step through the three-dimensional frames one by one up to 10+ min.

### 5.3. *Assessment of rockslide tsunami: Comparison with eyewitness accounts*

By adjusting the frictional coefficients such that the slide runs across Gilbert Inlet at about the same speed as the initial tsunami pulse wants to travel, the rockslide can indeed splash water to 500 m elevation as Miller observed. Although successfully reproducing the 525 m splash height has been the focus of previous investigations [Fritz *et al.* 2001; Mader, 1999; Mader and Gittings, 2002], we wish to go farther and assess model quality against additional eyewitness accounts and the mapped trimline around the bay. The eyewitnesses crewed two boats, the Edrie and the

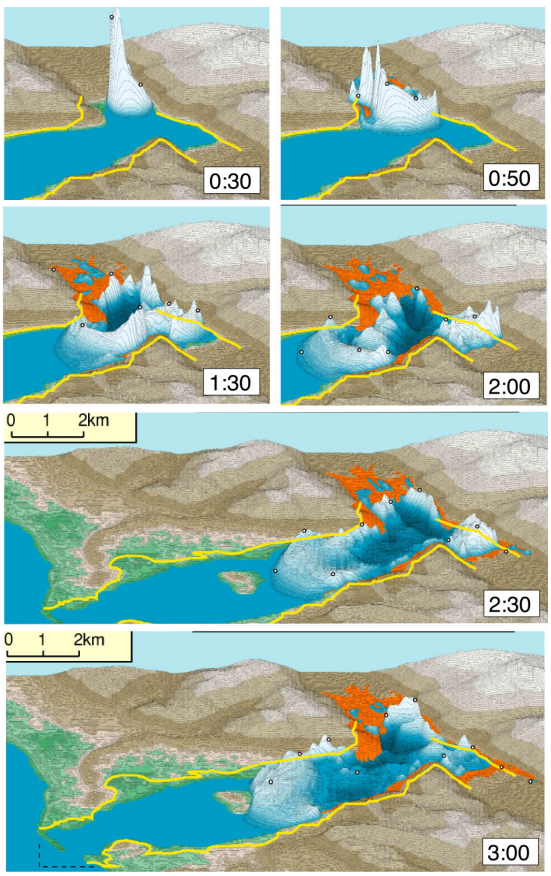


Fig. 7. Rockslide tsunami plotted in a three-dimensional style. Note that only a thin sheet of water climbs to several 100 m on the west slope of Gilbert Inlet (Frame B).

Badger, anchored at the western end of the bay near the southern and northern shores, respectively (Fig. 4).

**Edrie Account:** "*Midway between the head of the bay and Cenotaph Island the wave appeared to be a straight wall of water from shore to shore, possibly* 100 *feet* (30 m) *high in the center.*"

Assessment: The wave reaches this position at T $\sim$ 2 min (Fig. 6(a), Frame D.). The wave varies in height shore to shore from 10 m in the center to 20 m toward the south.

**Edrie Account:** "*When the wave reached the Edrie,* 2 *to* 3 *minutes after it was first sighted, the front appeared very steep and* 50 *to* 75 *feet* (15 – 25 m) *high.*"

Assessment: The wave reaches *Edrie*'s anchorage (Index K, Fig. 4) at T $\sim$ 4-1/2 min (Fig. 6(b), Frames C and D). Supposing that it took 1–1/1/2 min for the wave to exit Gilbert Inlet and be seen from *Edrie*, the model travel time of 3 min

seems consistent with observation. Rockslide wave height at the *Edrie* anchorage is about 10 m.

**Edrie Account:** "*The boat was carried toward and probably over the south shore and then, in the backwash, toward the center of the bay. The water surface returned to about normal level after the giant wave passed but was very turbulent, with much sloshing back and forth from shore to shore and with steep, sharp waves as much as* 20 *feet* (6 m) *high.*"

Assessment: The main wave passing *Edrie* is largely a single upward pulse of 45 s duration (Fig. 6(b), Frames D, E) and short period oscillations of 5–10 m persist to the ∼10 min end of simulation. The model does predict drawdown to −10 m after the passage of the wave (Fig. 6(b), Frame E). Although the motion of the boat toward the center of the bay indicates some return flow, the account makes no mention of seabed exposure from a large drawdown. Furthermore, the 10 m depth contour is 100 to 200 m offshore in this area and rocks and snags cover the seabed [U.S. Coast & Geodetic Survey 1942, 1969]. Likely, a 10 m drawdown would have dragged the *Edrie* across rough seabed and wrecked it.

**Badger Account:** "*The wave as it passed Cenotaph Island appeared to be about* 50 *feet* (15 m) *high in the center of the bay, and to slope upward toward the shores.*"

Assessment: The wave passes south of Cenotaph Island at T ∼ 3-1/3 to 4 min (Fig. 6(b), Frame C.). The wave varies height from 10 m at the Island mid-gap, to 17 m toward the south shore.

**Badger Account:** "*About* 4 *minutes after it was first sighted, the wave reached the Badger, stiff at anchor. The boat was lifted up and carried across La Chaussee Spit, riding stern first just below the crest of the wave, like a surfboard. Looking down at trees growing on the spit, I believe that I passed two boat lengths* (80 ft, 24 m) *over their tops.*"

Assessment: The wave approaches La Chaussee Spit at T ∼ 6 min. (Fig. 6(b), Frame E.). Supposing that it took 1–1/1/2 min for the wave to exit Gilbert Inlet far enough to be seen from the *Badger* at the Bay mouth, the 4-min timing seems adequate. The modeled waves at *Badger*'s anchorage (Location J, Fig. 4) peak at ∼7 m. Waves 5–6 m high crossed over the spit. Badger's report of an 80 foot breaking wave passing over the spit may be improbably large if, as stated, the wave was only 50 ft high as it passed through the narrows south of Cenotaph Island. Given that the eyewitness on the *Edrie* judged the wave as it passed Cenotaph Island as being significantly larger than the eyewitness on the *Badger*, it may be more plausible to accept the 80 ft height of the wave as it crossed La Chaussee spit rather than the 50 ft height at mid-bay. In any case, the rockslide only model significantly underestimates the size of the wave in the western end of the bay.

**Badger Account:** "*The wave crest broke just outside the spit and the boat hit bottom and foundered some distance from the shore. Looking back* 3 *to* 4 *minutes*

*after the boat hit bottom I saw water pouring over the spit, carrying logs and other debris. I do not know whether this was a continuation of the wave that carried the boat over the spit or a second wave.*"

Assessment: The rockslide model produces only a short duration wave over the sandspit rather than two positive waves or a sustained 3 to 4 min flood. By the end of the simulation at 10 min, water level in the western end of the bay falls close to its initial level again, apart from the confused short period waves noted from the *Edrie*. Flow over the spit has ceased well before this time.

Overall, the rockslide tsunami simulation conforms with the eyewitness observations, except for three main points:

(1) The simulated waves at the western end of the bay are rather smaller than estimated by most eyewitnesses: although this may not be significant, given the circumstances.
(2) The rockslide model forecasts significant drawdowns following the leading wave on the south side of the bay that likely would have dragged the *Edrie* on the rocks as it moved back into the bay.
(3) The rockslide only model produces a single, short duration flood over the sandspit, rather than two positive waves or a sustained flood.

### 5.4. *Assessment of rockslide tsunami: Comparison with the trimline*

Comparison of the mapped and model trimlines around the bay reveal other mismatches with the rockslide only model.

**Gilbert Head.** *The most notable feature of the trimline on Gilbert Head, other than its famous peak elevation of* 525 m, *is that on the east and west flanks of the headland, the trimline cuts diagonally across topographic contours* (*Fig.* 6(*a*), *Frame A*).

Assessment: As we noted, by adjusting its frictional coefficients, the rockslide can push water to $\sim$500 m elevation at positions close to peak trim. In fact, the highest run-up in the simulation (481 m) locates in landslide gully several 100 m north of the noted peak location. This gully is visible in Fig. 1(b). We don't know how deep it was in 1958 or whether Miller could define a trimline within it so we don't consider the difference in peak location to be a discrepancy. The diagonal trimline on eastern side of Gilbert Head can be matched because it directly faces the oncoming wave. Lower trimline heights up the valley of Lituya Glacier testify to the lower wave directivity in that direction. The 700-m-long diagonal trimline on the western side of Gilbert Head presents more of an enigma. Water topping the ridge has little velocity left otherwise it would keep on climbing. After topping, slow moving water wants to run straight down contours — not diagonally across (see mismatch between yellow trimline and orange inundation zone Fig. 6(a), Frame C). Miller [1960] paid particular attention to the flow pattern on Gilbert Head and claimed that flattened

trees on the western side were pointing parallel to the trim line and oblique to slope. For water to travel diagonally 700 m across contours on slope $\beta \sim 40°$ requires a very high ridge topping speed $V_{\text{top}}$. With constant down-slope acceleration of $g \cos \beta$, the down-slope deflection $\Delta P$ of a water bit would be

$$\Delta P = 0.5\, g \cos \beta \left[ \frac{700\,\text{m}}{V_{\text{top}}} \right]^2 \tag{34}$$

The term in brackets is just the time it takes for water to run down the 700 m trimline. It does not appear to us that the diagonal trim line deviates from straight by more than $\Delta P = 50$ m, so (34) gives a ridge topping velocity of 190 m/s! Such high-speed water would have splashed 100 s of meters further up on Gilbert Head than was observed. Possibly, like the model indicates, the upper part of the western diagonal was cut by topping water prior to it being turned down slope and a later (reflected) wave approaching more directly to that shore trimmed the bottom half.

**South Shore, East of Cenotaph Island — Mudslide Creek.** *On the South Shore, within a km or two east and west of Mudslide Creek, Miller mapped runups in the range of* 400–680 ft (120–210 m).

Assessment: The rockslide wave simulation gives a spot run-up of 209 m at $T = 1{:}38$ (View the movie to see this.) 2 km west of Mudslide Creek. Most locations on the south shore between Crillon Inlet and this location suffered runups of 100–150 m in the model, rather less than the trimline mapping.

**North Shore, East of Cenotaph Island.** *On the North Shore east of Cenotaph Island, mapped runups range from* 90–225 ft (25–70 m). *Run-in reached* 600 m *on a shoreline projection north of the Island.*

Assessment: The rockslide tsunami well matches the trimline information on this part of the shore.

**Cenotaph Island.** *On the west and east sides of Cenotaph Island, Miller mapped runups in the range of* 40–80 ft (12–25 m) *and* 40–160 ft (12–50 m) *respectively.*

Assessment: Run-ups on the west and east sides of Cenotaph Island in the rockslide tsunami simulation reached 30–40 m and 25–30 m. The simulation produced higher run-up on the back (west) side of the Island as the wave boomeranged around from the south and converged with the wave from the north. Backside amplification from "Island Wrap Around" is common in tsunami studies but it did not occur here.

**North Shore, West of Cenotaph Island — Fish Lake.** *On the North Shore, within* 2 km *of Fish Lake, mapped run-ups range from* 80–120 ft (25–35 m). *Maximum mapped run-in distance for the tsunami was* 1400 m *here.*

Assessment: The rockslide tsunami simulation does a good job in reproducing trimline information on this part of the shore.

**South Shore, West of Cenotaph Island.** *On the south shore, south and west of Cenotaph Island, Miller's run-ups range between* 85 *and* 130 ft (25–40 m). *Run-in distances along this stretch were* 300–400 m.

Assessment: The rockslide tsunami does a poor job in matching trimlines on this part of the south shore. Model run-ups are generally less than 25 m and run-ins less than about 100 m.

Although the rockslide model successfully reproduced the $\sim 500$ m splash, in our assessment, the wave size and inundation on the south shore and at the western end of Lituya Bay are a bit anemic relative to the eyewitness and trimline accounts.

How could the rockslide wave run-up $\sim 525$ m on Gilbert Head yet be too small further away? Understand that the rockslide directs the primary wave pulse along the line of the fall, almost due west. This directivity enables the 525 m high splash on Gilbert Head as the wave pulse breaks on shore, but less efficiently sends waves in other directions. Waves travelling south, for example, shed off the flank of the slide rather than its front, so southbound waves start off smaller than the westbound waves ($\sim 35$ vs. $\sim 100$ m). You can clearly see the size difference in Fig. 7, Frames A, B. Moreover, to reach the western end of Lituya Bay, southbound waves must bend around Gilbert Head, a process that further reduces their size to 15–20 m. Now true, a still larger volume rockslide could increase wave size outside of Gilbert Inlet, but the simulation already employs a slide at the top end ($5.5 \times 10^7$ m$^3$) of the likely volume. (Our attempt to beef-up the rockslide tsunami toward the west, was the motivation for selecting a volume higher than Miller's $3 \times 10^7$ m$^3$ estimate.)

We conclude that it is unlikely, although not impossible, that the rockslide tsunami alone could have been sufficiently large to match all of the eyewitness and trimline accounts. Certainly, enough discrepancies exist beyond Gilbert Inlet to spur speculation about other factors that may have contributed to the 1958 Lituya Bay tsunami.

## 6. Bathymetry Changes in Pre- and Post-1958 Surveys: Evidence for a Sub-Glacial Landslide

Miller's depiction of the pre-1958 [Miller 1960, Plate 2, and red dashed contours Fig. 8 top] bathymetry of Lituya Bay includes a broad expanse from east of Cenotaph Island to Gilbert Inlet sounding from 500 to 720 feet (150–220 m). Oddly however, in post-1958 surveys, this extensive deep region vanished. In fact, a 1969 chart based on a 1959 survey, [U.S. Coast and Geodetic Survey 1969; yellow and green area Fig. 8 top] reveals a remarkably flat bottom at 75–78 fathoms (450–470 ft, 137–143 m) with only a slight ridge separating two subbasins; a small one at the T junction south of Gilbert Head, and a larger one curved around Cenotaph Island. By comparing the 1942 and 1969 maps, we calculate that $\sim 3 \times 10^8$ m$^3$ of material flowed into the fiord, blanketing the entire area within the 130 m depth contour with up to 70 m of infill (50 m average over 6 km$^2$ = 0.3 km$^3$). In the absence of a seismic/coring survey of the bay bed, the date of infilling cannot be constrained within the 1926 and 1959 surveys. Possibly, the infilling spanned years as sediment graded out from the glacier deltas. Fortunately, a third survey published in 1990

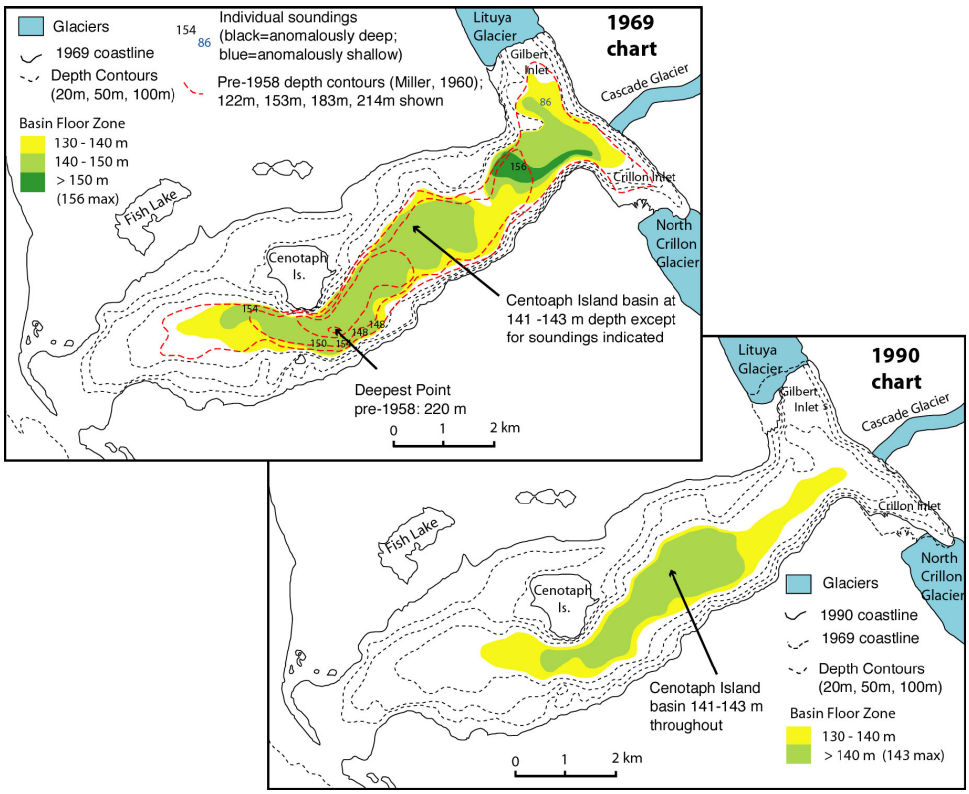


Fig. 8. Evolution of Lituya Bay bathymetry as revealed by successive U.S. Coast & Geodetic Survey charts. (Top) A 1969 chart based on a 1959 survey shows the floor of the bay to be remarkably flat, in contrast to the deep trough evident in pre1958 data (red dashed lines) contoured by Miller [1960]. (Bottom) A chart published in 1990 shows infilling by sediment at either end of the bay but little change in the central part of the bay.

(Fig. 8, bottom) [U.S. Coast and Geodetic Survey, 1990] allows us to gauge infill rates. Indeed, chart changes from 1942 to 1969 differ radically from those between 1969 and 1990. From 1969 to 1990, the eastern subbasin close to the proglacial deltas infilled and a continuous gentle slope formed between the deltas and the Cenotaph Island basin. However, except for the disappearance of anomalously deep areas along the south side, the Cenotaph Island subbasin shallowed by only 1–3 m in the time period. In contrast, the bulk (90 to 95%) of the depth changes between 1942 and 1969 concentrated in the center of the bay rather than at the ends of the bay near the sediment sources as does the 1969–1990 pattern. Infilling near the center of bay implies energetic sediment transport event(s) during 1942–1969.

Having no reason to think that the secular sedimentation rate from 1942 to 1969 differs from the 1969 to 1990 rate, we are left with the notion that most of the infill happened quickly, sometime between the 1929 and 1959 surveys. Recognizing that events of July 9, 1958 were the region's most violent happenings in that interval,

we propose that the infilling was contemporaneous with the quake, rockslide, and tsunami. If this is so, where could $3 \times 10^8\,\mathrm{m}^3$ of material have originated? Recall that the rockslide contained 3–$6 \times 10^7\,\mathrm{m}^3$ of material, just 10–20% of the infill volume. Miller [1960] reckoned that the tsunami eroded an additional $\sim 4 \times 10^6\,\mathrm{m}^3$ of soil, subsoil, glacial sediment and, bedrock. The additional eroded matter could not have contributed more than a few percent of the infill. A small tsunami did occur in 1936 in the southern arm of the bay opposite Gilbert Inlet [Miller, 1960]. Miller mapped its trimline and concluded that the 1936 wave was about one-tenth the size of the 1958 tsunami. Being so small, deposits from the 1936 landslide could not have contributed much to the bathymetry changes between 1929 and 1959. Seeing no other candidates for the infill, we submit that the material originated from underneath the foot of Lituya Glacier during the 1958 event.

Figure 9 cartoons our "dual-slide" scenario. As little as 10 s after being triggered, the rockslide impacts Lituya Glacier, shattering its tip (Fig. 9, Frames A and B). Between 10 and 25 s, the rockfall gouges a cavity on the inlet floor under the glacier front (Fig. 9, Frame C). As discussed in Sec. 1, before and after photos document that $\sim 400$ m of the glacier and its substrate were no longer in place after the rockslide, so these first steps have observational support. For the next step, we hypothesize that rockslide scouring action destabilized the subglacier foundation, creating a "dam break" of water-saturated sediment further up-slope that may have been weakened by earthquake shaking. Released subglacier material began to pour out from under the broken glacier tip with the head scarp of the instability working its way several 100 m up-slope in a minute or so (Fig. 9, Frame D). During or after this retrogressive failure, having lost part of its central foundation, Lituya Glacier collapsed leaving many prominent cracks and normal faults (Fig. 9, Frame E). Miller noted that several 100 m of Lituya Glacier upstream of the new termination appeared more faulted than it did a few days earlier (Fig. 1(b)), so a partial glacier collapse has observational footing. One puzzle is the preservation of the faulted glacier — it might be expected to disintegrate and exit with the subglacier flow. Possibly, subglacial water separated the ice from the underlying sediment. With limited coupling between the central glacier and sediment below, the exiting material may not have been able to drag the ice along, especially if the glacier was well grounded at the edges.

Alternative to Frame C in Fig. 9, the subglacial slide could have been triggered directly by earthquake shaking. Failure by this method however, could occur any time between the start of shaking and hours after owing to the delay in pore fluid pressure buildup [Biscontin *et al.*, 2004]. While direct triggering is possible, a delay of the subglacial slide by more than a couple of minutes would result in two distinct tsunami waves, contrary to the observations from the *Edrie*.

We believe that pre- and post-1958 bathymetry suggests that the Lituya Bay tsunami had a "dual slide" source. Triggered soon after the visible rockslide, a large, generally invisible, submarine slide emerged from under Lituya Glacier, progressed southward down Gilbert Inlet and eventually infilled the deeper regions of

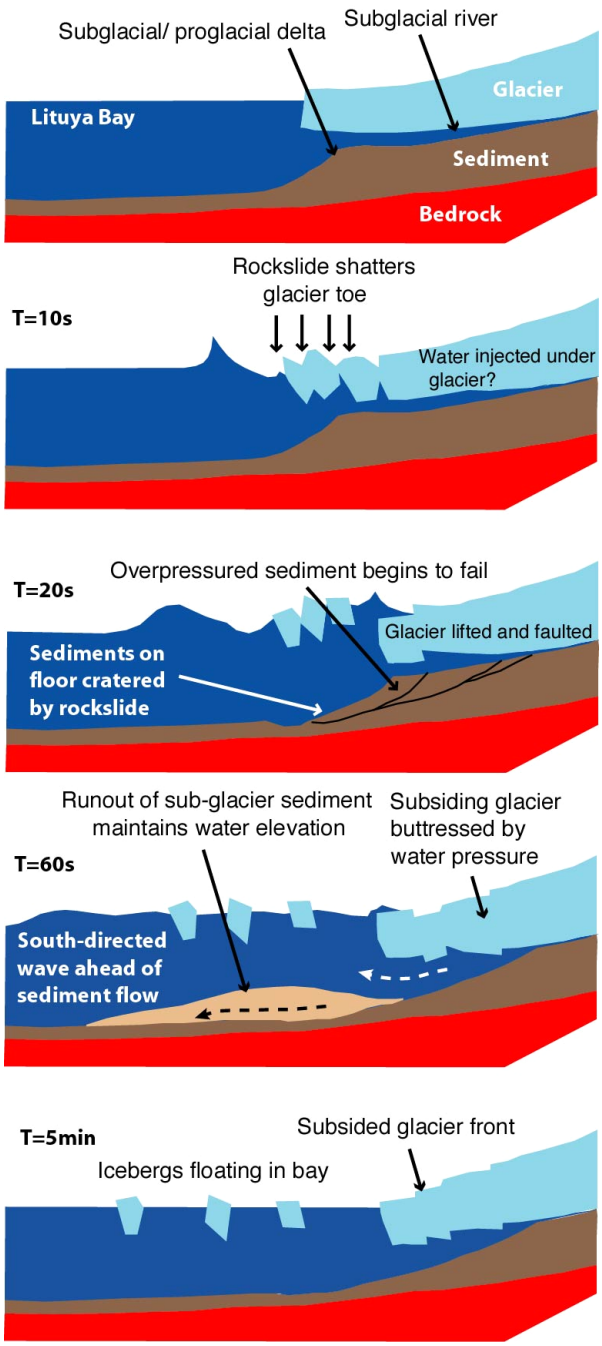


Fig. 9. Proposed sequence of events in N-S cross-section through the axis of Lituya Glacier. (A) Initial state. (B) Rockslide impact and loss of glacier tip. (C) Failure of overpressured sediment under the glacier. (D) Release and outflow of subglacier sediment, enhancing south-directed wave. (E) Final state with subsided and faulted glacier.

Lituya Bay. Similarly the subglacier material moved more slowly than the rockfall, but because it possessed a greater volume and flowed southward not westward, the tsunami outside of the Inlet should increase in size relative to the rockslide only case.

## 7. 1958 Lituya Bay Landslide Tsunami — Dual Slide Source

### 7.1. *Landslide parameters and landslide evolution*

For our dual slide simulation, the rockslide maintains its original parameters. We suppose that the subglacier slide coincides with the 1.5 km square region covering the missing glacier tip plus the area of fresh normal faults. We give the subglacier slide a volume of $2.2 \times 10^8\,\mathrm{m}^3$ such that this, combined with the rockslide volume totals the $\sim 3 \times 10^8\,\mathrm{m}^3$ of infill needed to explain the observed bathymetric changes between 1942 and 1969. The material in the subglacier slide (area: $2.46 \times 10^6\,\mathrm{m}^2$) slightly mounds along the axis of the glacier and tapers off toward its flanks. The 90 m mean thickness of the simulated glacier slide accommodates easily in the space between sea level and the $\sim$130 m deep toe of the proglacial delta prior to 1958. Basal, $C_\mathrm{b}$ and dynamic drag $C_\mathrm{d}$ coefficients for the subglacier material equal those for the rockslide. The subglacier slide initiates at $T = 15$ s, shortly after the rockslide hits the floor of Gilbert Inlet. Self-topography eases in over 90 s for the subglacier slide as it disaggregates into granular sediment. The dual slide consists of 45,000 bits stepped at 1 s intervals.

Figures 10(a) and 10(b) sequence the dual slide simulation. (Quicktime movie at http://es.ucsc.edu/∼ward/lituya-dualslide.mov).

$\Rightarrow T$: 0–30 s (Fig. 10(a) Frames A, B): The rockslide descends from its high perch and runs across Gilbert Inlet as before. The sub-glacier slide, released at 15 s, begins to show movement.

$\Rightarrow T$: 30–60 s (Fig. 10(a) Frame C): The subglacier slide surges southward and hits a top speed of about 25 m/s.

$\Rightarrow T$: 1–4 min (Fig. 10(b) Frames A–D): The subglacier slide deforms into a debris flow and slows to 10 m/s as it encounters the divide between the main arm of the fiord and Crillion Inlet.

$\Rightarrow T$: 4–15+ min (Fig. 10(b) Frames D, E): Over the next 15–20 min, the low strength debris flow marches the length of Lituya Bay and settles into deepest region of the fiord. The bottom rises by 60 m in the Cenotaph Island subbasin but scant shallowing occurs near the head of the bay. The flat expanse so generated (Fig. 10(b), Frame F) explains the differences in pre- and post-1958 bathymetry. Contrast the upper left and lower right frames of Fig. 10(b).

The dual slide releases $3 \times 10^{15}$ J of potential energy — three times that of the rockslide alone.

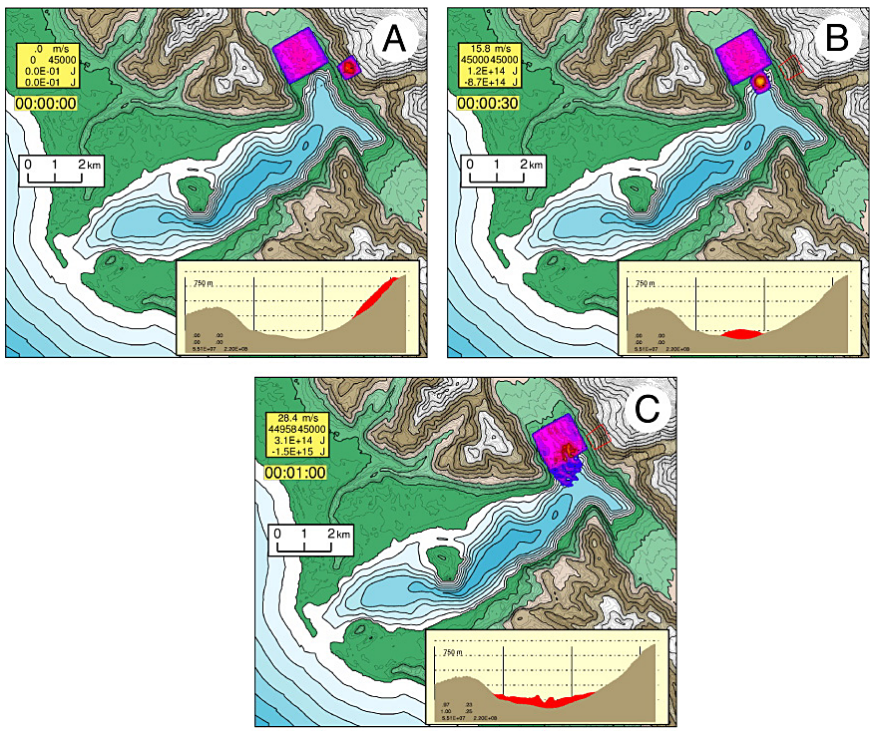


Fig. 10(a). Dual slide simulation at $T = 0$, 30, and 60 s.

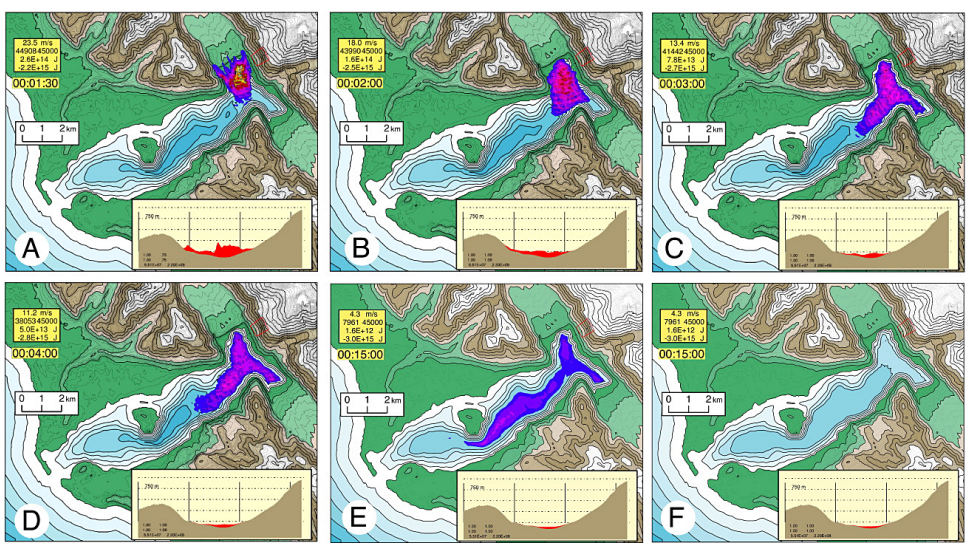


Fig. 10(b). Dual slide at $T = 11/2, 2, 3, 4$, and 15 min. Note the flat final state of the fiord floor at depth of 130–150 m, some 60 m shallower than prior to the slide. Contrast the upper left and lower right frames.

### 7.2. *Wave simulation for the dual slide source*

Figures 11(a) and 11(b) picture tsunami from the dual slide simulation in two-dimensional map view, with the same wave height contours as in Fig. 6. (Corresponding Quicktime movie at http://es.ucsc.edu/∼ward/lituya2d-dual.mov).

⇒ $T$: 0–60 s (Fig. 11(a): Frames A, B): The initial sequence of events including the splash to ∼500 m are essentially unchanged from the rockslide model in Fig. 5.

⇒ $T$: 1–2 min (Fig. 11(a): Frames C, D): From this time onward, the increase in tsunami size due to the subglacier slide becomes apparent. Compare the "whiteness" of Fig. 11 outside of Gilbert Inlet with Fig. 6. Note the 50–55 m high waves generated by dual slide bearing down on the south shore in Frame D, vs. 35 m high ones from the rockslide.

⇒ $T$: 2–4 min (Fig. 11(b): Frames A, B): Water runs up over 200 m on the south shore in the area of Mudslide Creek. Contrast 150 m run-up for the rockslide tsunami.

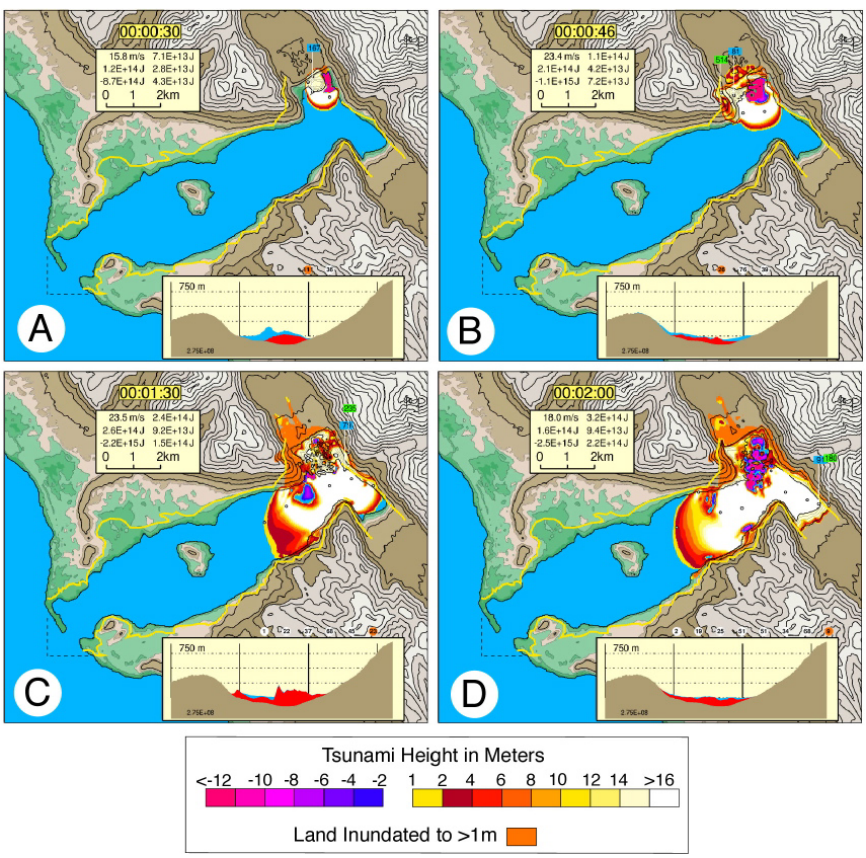


Fig. 11(a). Dual slide tsunami simulation at $T = 30$ s, 46 s, 1–1/2 min, and 2 min.

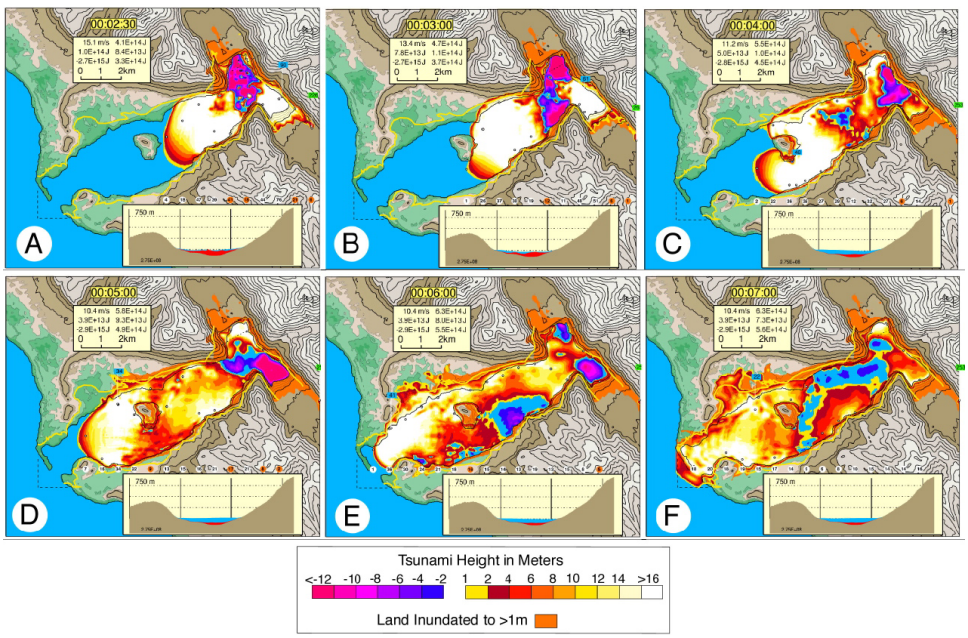


Fig. 11(b). Tsunami for dual slide source $T = 2 - 1/2, 3, 4, 5, 6$, and 7 min.

$\Rightarrow T$: 4–5 min (Fig. 11(b): Frame C): A 30–35 m high wave strikes the east face of Centotaph Island, running up on land to 60 m. Contrast 20 m waves striking the Island and 40 m run up for the rockslide tsunami.

$\Rightarrow T$: 5–6 min (Fig. 11(b): Frame D): The branch of the wave passing south Cenotaph Island reaches 30 m and refracts north to combine with northern branch. The combined waves peak at 35 m and run-in 1–2 km on the North Shore near Fish Lake.

$\Rightarrow T$: 6–7+ min (Fig. 11(b): Frame E): Twenty meter size waves approach and override La Chaussee Spit and 10 m waves escape to the sea. Contrast 10 m and 5 m for the rockslide only.

Figure 12 shows the dual-slide tsunami in a three-dimensional style at $T = 1, 3, 5$, and 7 minutes. (Quicktime movie at http://es.ucsc.edu/∼ward/lituya3d-dual.mov). It is obvious that the subglacier slide has beefed-up tsunami size outside of Gilbert Inlet (Compare the $T = 3$ min frames in Figs. 6(b) and 11(b)).

### 7.3. *Assessment of dual slide tsunami: Comparison with eyewitness accounts*

**Edrie Account:** "*Midway between the head of the bay and Cenotaph Island the wave appeared to be . . . possibly* 100 *feet* (30 m) *high in the center.*"

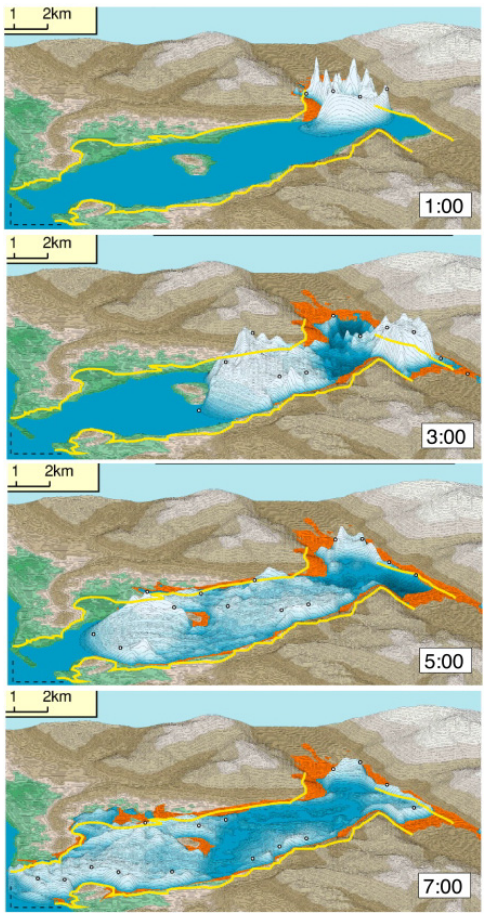


Fig. 12. Dual slide tsunami plotted in a three-dimensional style.

Assessment: The wave reaches this position at $T \sim 2$ min. (Fig. 11(a), Frame D.) The wave varies in height from 20 m in the bay center to 40 m on the south shore. The dual slide better fits this observation than the rockslide only.

**Edrie Account:** "*When the wave reached the Edrie,... the front appeared very steep and* 50 *to* 75 *feet* (15–25 m) *high.*"

Assessment: The height of the steep wave front approaching the Edrie anchorage is $\sim 18$ m, a good match.

**Edrie Account:** "*The water surface returned to about normal ... with much sloshing ... and with steep, sharp waves as much as* 20 *feet* (6 m) *high.*"

Assessment: The main wave passing the *Edrie* is largely a single upward pulse of $\sim 60$ s duration (Fig. 11(b), Frames D–F), longer than in the rockslide only model. Further, only a small drawdown follows, consistent with the eyewitness observation

and the survival of the boat as it was transported back out over the shallow seabed from the shore. Oscillations of 5–10 m persist to the ∼10 min end of simulation.

**Badger Account:** "*The wave as it passed Cenotaph Island appeared to be about* 50 *feet* (15 m) *high in the center of the bay...*"

Assessment: The wave passes south of Cenotaph Island at about $T \sim$ 3-1/2–4 min (Fig. 11(b), Frame C). The wave height reaches 30 m near the shores and a little less in mid-channel.

**Badger Account:** "*across La Chaussee Spit...I believe that I passed two boat lengths* (24 m) *over the tree tops.*"

Assessment: The wave exceeds 15 m as it crosses the spit. Overall, the dual slide model conforms with the estimated wave height from the *Edrie* and the *Badger* as it was swept across the spit.

**Badger Account:** "*The wave crest broke just outside the spit and the boat hit bottom...*3 *to* 4 *min after the boat hit bottom I saw water pouring over the spit...I do not know whether this was a continuation of the wave that carried the boat over the spit or a second wave*".

Assessment: The dual slide model produces a sustained flow over the spit that continues to the end of the simulation at 10 min, consistent with this observation.

As a whole, the dual slide model better fits most of the eyewitness observations than does the rockslide only model, particularly those relating to the size and duration of the tsunami in the western end of the bay.

### 7.4. *Assessment of dual slide tsunami: Comparison with mapped trimline*

**Gilbert Head.** The dual slide model produces run-ups similar to the rockslide only model. Again, slowly traveling tsunami balls topping the ridge descend the south-facing slope perpendicular to contours.

Assessment: The lack of difference between the two models testifies that the rockslide is responsible for tsunami effects on Gilbert Head. Both models fail to produce the oblique-to-slope trimline and flattened trees on the western slope of Gilbert Head.

**South Shore, East of Cenotaph Island — Mudslide Creek.** Dual slide run-ups of 120–200 m in this sector exceed those in the rockslide only model.

Assessment: The dual slide model run-ups are close to observed values.

**North Shore, East of Cenotaph Island.** Dual slide model run-ups here are 25–70 m, whilst model run-in reached 600 m.

Assessment: These values are similar to those observed.

**Cenotaph Island.** Model run-ups on the western and eastern sides of Cenotaph Island are 12–25 m and 12–50 m, respectively.

Assessment: The dual slide model produces higher run-ups on the eastern side than on the western side of Cenotaph Island, consistent with the field observations. The reverse applies to the rockslide only model.

**North Shore, West of Cenotaph Island — Fish Lake.** Here, the dual slide model produces run-ups of 25–35 m and a maximum run-in of 2000 m.

Assessment: The run-in at Fish Lake may be excessive. Model run in is sensitive to the choice of onshore basal drag friction. Perhaps $C_b$ ought to be increased given that the dense forest growing here in 1958 may have slowed the inundation and reduced its reach.

**South Shore, West of Cenotaph Island.** The dual slide model runs up 25–40 m and runs in 300–400 m here.

Assessment: These values, though larger than those in the rockslide model, still fall short of the mapped trimline in places, notably in the area south of Cenotaph Island.

Overall, by including the subglacier slide, tsunami heights and runups beyond Gilbert Inlet increase by 50–100% relative to those from the rockslide alone. Mostly, the dual slide wave better fits the trimline data and eyewitness accounts than the rockslide only wave. In a few cases, the predicted dual slide tsunami borders on extreme. We can always reduce the contribution of the subglacier slide to the tsunami by increasing its frictional coefficients and slowing its failure. We could also admit spatially variable on land dynamic friction coefficient $C_d$ in locations of excess inundation.

## 8. Destabilization of Proglacial and Subglacial Sediments by Rockslides: Is this Realistic?

The addition of a submarine slide of subglacial and proglacial sediment with 5 to 10 times the volume of the initial subaerial rockslide improves the fit of model tsunami and explains the infill of the bay between 1942 and 1969. All well and good, but is this mechanism realistic? Have such large entrainment ratios occurred elsewhere in similar terrains? In fact — yes, a number of recent rockslides in glaciated valleys have impacted glaciers and glacial sediments and "bulked up" in volume many times over by incorporation of ice and sediment. Notable cases comparable to Lituya Bay include:

(1) The September 20, 2002 *Kolka-Karmadon* rock and ice landslide in the Caucasus mountains [Kaab *et al.*, 2003]. An initial rock/ice slide of 10 to 20 million $m^3$ entrained $\sim$100 million $m^3$ of ice and sediment as it impacted the Kolka glacier on the valley floor. Subsequent debris flows and lahars traveled 33 km. The bulking ratio of 5 to 10 compares to that inferred for Lituya Bay.

(2) The November 29, 1987 *Parraguirre* landslide in central Chile [Hauser, 2002]. An initial $6 \times 10^6\,\mathrm{m}^3$ rockslide entrained glacigenic sediments on the valley floor producing a far-traveled debris flow with volume $15 \times 10^6\,\mathrm{m}^3$ and bulking ratio of 2.5. (see http://es.ucsc.edu/∼ward/parraquirre.mov).
(3) The May 31, 1970 *Huascaran* landslide in Peru [Plafker and Ericksen, 1975]. This began with a $13 \times 10^6\,\mathrm{m}^3$ rock and ice landslide that entrained sediment downslope for a final volume of $50 \times 10^6\,\mathrm{m}^3$. The bulking ratio is of around 4.

Erismann and Abele [2001], Scott *et al.*, [2001], McSaveney [2002], Hungr and Evans [2004], and Huggel *et al.* [2008] discuss other landslides in glaciated and mountainous terrains with significant but less well constrained bulking by ice and sediment. Other than Lituya Bay, we are not aware of subaerial rockslides inducing underwater landslides. Still, being fully water saturated, submarine or unfrozen subglacial sediments may be particularly susceptible to the process. Hazard assessments for tsunami in fjords should allow for the possibility of submarine landslides in proglacial or subglacial sediments triggered by subaerial rockslides.

## 9. Conclusions

This article introduces a new tack to tsunami generation and inundation. It uses a momentum equation to accelerate balls of water over variable depth topography and it computes water surface height from the volume density of nearby balls. Compared with finite element/finite difference approaches, tsunami balls are more intuitive plus they have the advantages that: the continuity equation is satisfied automatically; the procedure is meshless; and that inundation is simply tsunami balls run onto land.

We demonstrate and validate the tsunami ball method by simulating the 1958 Lituya Bay landslide and tsunami. We find that a rockslide of size and volume generally in accord with observations can indeed tumble from 200 to 900 m height on the east slope of Gilbert Inlet, drive a sheet of water up to $\sim 500$ m on the western slope, and make an impressive tsunami running down the length of the fiord. A closer examination of the eyewitness and trimline accounts however, finds a "rockslide only" tsunami lacking in size outside of Gilbert Inlet. This discrepancy coupled with the observation that $\sim 3 \times 10^8\,\mathrm{m}^3$ of material in-filled Lituya Bay between 1942 and 1969, suggests that the 1958 tsunami originated from not one landslide, but two. The first was the rockslide that generated the famous big splash. Shortly after, proglacial and subglacial sediment under Lituya Glacier destabilized by the impact of falling rocks, surged southward in a second, larger, and slower moving submarine slide. The subglacier slide induced the fresh normal faults on the collapsed glacier above, helped to bulk up the rockslide tsunami outside of Gilbert Inlet, and contributed the lion's share to the observed post-1958 infill on the floor of the bay.

Although we cannot prove that a subglacier slide happened, the bathymetry changes and the lower-than-observed size of the rockslide only tsunami point in

that direction. If nothing else, our study warrants a new seismic and coring survey of the Lituya Bay subbottom to verify or disprove the presence of a 70 m thick unit of reworked glacigenic sediment contemporaneous with 1958 earthquake and tsunami backwash deposits.

**Appendix A.** Quicktime movie links to the simulations presented in this article.

Rockslide:
http://es.ucsc.edu/∼ward/lituya-slide.mov

Rockslide Tsunami 2D:
http://es.ucsc.edu/∼ward/lituya2d.mov

Rockslide Tsunami 3D:
http://es.ucsc.edu/∼ward/lituya3d.mov

Dual Slide:
http://es.ucsc.edu/∼ward/lituya-dualslide.mov

Dual Slide Tsunami 2D:
http://es.ucsc.edu/∼ward/lituya2d-dual.mov

Dual Slide Tsunami 3D:
http://es.ucsc.edu/∼ward/lituya3d-dual.mov

Other 3D views not included in this paper
http://es.ucsc.edu/∼ward/lituya-2000.mov
http://es.ucsc.edu/∼ward/lituya-escape.mov
http://es.ucsc.edu/∼ward/lituya-4m.mov
http://es.ucsc.edu/∼ward/lituya-es-dir.mov

## References

Biscontin, G., Pestana, J. M. and Nadim, F. [2004] "Seismic triggering of submarine slides in soft cohesive soil deposits," *Marine Geology* **203**, 341–354.

Erismann, T. H. and Abele, G. [2001] *Dynamics of Rockslides and Rockfalls* (Berlin, Springer-Verlag).

Fritz, H. M. [2002] Initial phase of landslide generated impulse waves, Ph.D. thesis ETH-No. 14871, Swiss Federal Institute of Technology, ETH Zurich, Switzerland.

Fritz, H. M., Hager, W. H. and Minor, H-E. [2001] "Lituya Bay case: Rockslide impact and wave run-up," *Sci. Tsunami Hazards* **19**(1), 3–22.

Fritz, H. M., Mohammed, F. and Yoo, J. [2009] "Lituya Bay landslide impact generated mega-tsunami 50th anniversary," *Pure Appl. Geophys.* **166**(1–2), 153–175, DOI 10.1007/S00024-008-0435-4.

Hauser, A. [2002] Rock avalanche and resulting debris flow in Estero Parraguirre and Rio Colorado, Region Metropolitana, Chile. In: Evans, S. G. and DeGraff, J. V. (eds.). *Catastrophic Landslides: Effects, Occurrence and Mechanisms*, Colorado, Boulder. *Geol. Soc. Am. Rev. Eng. Geology* **15**, 135–148.

Hungr, O. and Evans, S. G. [2004] "Entrainment of debris in rock avalanches: An analysis of a long run-out mechanism," *Geol. Soc. Am. Bull.* **116**, 1240–1252.

Jiang, L. and LeBlond, P. H. [1993] "Numerical modeling of an underwater Bingham plastic mudslide and the waves which it generates," *J. Geophys. Res.* **98**, 10313–10317.

Kaab, A., Wessels, R., Haeberli, W., Huggel, C., Kargel, J. S. and Khalsa, S. J. S. [2003] "Rapid ASTER imaging facilitates timely assessment of glacier hazards and disasters," *Eos* **84**(13), 117, 121.

Lynett, P. and Liu, P. L. F. [2003] "A numerical study of submarine landslide–generated waves and runup," *Proc. Royal Soc. London, Coast Ocean Eng.* A, **458**, 2885–2910.

Mader, C. L. [1999] "Modeling the 1958 Lituya Bay mega-tsunami," *Sci. Tsunami Hazards*, **17**(1), 57–67.

Mader, C. L. and Gittings, M. L. [2002] "Modeling the Lituya Bay mega-tsunami II," *Sci. Tsunami Hazards*, **20**(5), 241.

McSaveney, M. J. [2002] "Recent rockfalls and rock avalanches in Mount Cook National Park, New Zealand. In: Evans, S. G. and DeGraff, J. V. (eds.), *Catastrophic Landslides: Effects, Occurrence and Mechanisms*, Colorado, Boulder. *Geol. Soc. Am. Rev. Eng. Geology* **15**, 35–70.

Miller, D. J. [1960] Giant waves in Lituya Bay, Alaska, *U. S. Geol. Survey, Prof. Paper 354-C*, 51–86.

Miller, D. J. [1964] "The Alaska earthquake of July 10, 1958: Giant wave in Lituya Bay," *Bull. Seis. Soc. Am.* **50**(2), 253–266.

Plafker, G. and Ericksen, G. E. [1978] Nevados Huascaran avalanches, Peru. In: *Rockslides and Avalanches I: Natural Phenomena*, Voight, B. (ed.). Amsterdam, Elsevier, pp. 277–314.

Rodgers, B. D. and Dalrymple, R. A. [2008] SPH modeling of tsunami waves, Chapter 3. In *Advanced Numerical Models for Simulating Tsunami Waves and Runup*, Liu, P. L. F., Yeh, H. and Synolakis, C. (eds.), Singapore, World Scientific Publishing.

Satake, K. [1995] "Linear and non-linear computations of the 1992 Nicaragua earthquake tsunami," *Pure Appl. Geophysics* **144**, 455–470.

Satake, K. [2007] "Volcanic origin of the 1741 Oshima-Oshima tsunami in the Japan Sea," *Earth Planets Space* **59**, 381–390.

Scott, K., Macias, J. L., Naranjo, J. A., Rodriguez, S. and McGeehin, J. P. [2001] Catastrophic debris flows transformed from landslides in volcanic terrains: Mobility, hazard assessment and mitigation strategies. *U. S. Geol. Survey Prof. Paper* 1630.

Titov, V. V. and Gonzalez, F. I. [1997] Implementation and test of the method of splitting tsunami (MOST) model, *NOAA Technical Memorandum ERL PMEL-112*, 14 pp.

Ward, S. N. [2009] "A tsunami ball approach to storm surge and inundation: Application to hurricane Katrina," *Int. J. Geophysics*, **2009**, Article ID 324707, 13 pp., DOI 10.1155/2009/324707.

Ward, S. N. and Day, S. [2006] "A particulate kinematic model for large debris avalanches: Interpretation of debris avalanche deposits and landslide seismic signals of Mount St. Helens, May 18th 1980," *Geophys. J. Int.*, **167**, 991–1004, DOI:10.1111/j.1365-246X.2006.03118.x.

Ward, S. N. and Day, S. [2008] "Tsunami balls: A particulate approach to tsunami runup and inundation," *Comm. Comput. Phys.*, **3**, 222–249.

United States Coast and Geodetic Survey [1942] Chart 8505, Lituya Bay.

United States Coast and Geodetic Survey [1969] Chart 8505, Lituya Bay.

United States Coast and Geodetic Survey [1990] Chart 16762, Lituya Bay.